Upper mantle mush zones beneath low melt flux ocean island volcanoes: insights from Isla Floreana, Galápagos

Matthew L. M. Gleeson[1]*, Sally A. Gibson[1] and Michael J. Stock[1,2]

[1]Department of Earth Sciences, University of Cambridge, Downing Street, CB2 3EQ, UK

[2]Department of Geology, Trinity College Dublin, College Green, Dublin 2, Ireland.

*Corresponding author email address: mlmg3@cam.ac.uk

ABSTRACT

The physicochemical characteristics of sub-volcanic magma storage regions have important implications for magma system dynamics and pre-eruptive behaviour. The architecture of magma storage regions located directly above high buoyancy flux mantle plumes (such as Kīlauea, Hawaii and Fernandina, Galápagos) are relatively well understood. However, far fewer constraints exist on the nature of magma storage beneath ocean island volcanoes that are distal to the main zone of mantle upwelling or above low buoyancy flux plumes, despite these systems representing a substantial proportion of global ocean island volcanism. To address this, we present a detailed petrological study of Isla Floreana in the Galápagos Archipelago, which is characterised by an extremely low flux of magma into the lithosphere from the underlying mantle plume. Detailed *in situ* major and trace element analyses of crystal phases within exhumed cumulate xenoliths, lavas and scoria deposits, indicate that magma storage beneath Floreana is dominated by crystal-rich domains (i.e. mush). Trace element disequilibria between cumulus phases and erupted melts, as well as trace element zoning within the xenolithic clinopyroxenes, reveals that reactive porous flow (previously identified beneath mid-ocean ridges) is an important process of melt transport within these crystal-rich storage regions. In addition, application of three petrological barometers reveal that the Floreana mush zones are located in the upper mantle, at a depth of 23.7±5.1 km. Our barometric results are compared to recent studies of high melt flux volcanoes in the western Galápagos, Hawaii and Iceland, and demonstrate that the flux of magma from the underlying mantle source represents a first-order control on the depth and physical characteristics of magma storage beneath ocean island volcanoes.

KEY WORDS

Galápagos; magma storage; reactive porous flow; barometry.

1 INTRODUCTION

The physicochemical characteristics (such as size, pressure, volatile content and geochemical heterogeneity) of magma storage at volcanic centres located directly above high buoyancy flux mantle plumes (e.g. Kīlauea, Hawaii and Isabela, Galápagos) have been subject to intense study over the past few decades (Bagnardi et al., 2013; Clague and Denlinger, 1994; Geist et al., 1998; Naumann and Geist, 1999; Park et al., 2007; Pietruszka et al., 2015; Poland et al., 2015; Stock et al., 2018; Wieser et al., 2020, 2019). Systems such as Kīlauea are characterised by frequent volcanic activity, and geophysical (seismicity, ground deformation) and geochemical (gas emissions) monitoring is prevalent. Monitoring data, combined with petrological and geochemical analysis of erupted products (mineral textures, deformation characteristics and chemistry) provide important insights into the architecture and dynamics of their sub-volcanic plumbing systems (Amelung et al., 2000; Davidge et al., 2017; Geist et al., 2014; Hartley et al., 2018; Kilbride et al., 2016). However, these systems (which we term 'high melt flux') represent only one endmember of global plume-derived volcanism. Low melt flux systems, either above low buoyancy flux plumes (e.g. Canary Islands; Longpre et al., 2014) or at volcanic systems distal to the centre of mantle melting at high buoyancy flux mantle plumes (e.g. eastern and southern Galápagos; Harpp and Geist, 2018), are the other endmember.

Although a substantial number of Holocene hotspot-related volcanic systems are located in regions characterised by a relatively low flux of magma into the lithosphere (e.g. Samoa, Canary Islands, Cape Verde; Global Volcanism Program, 2013), only a small number of eruptions have been observed (and recorded) at these systems since the advent of modern volcano monitoring techniques. As a result, few constraints exist on the conditions of magma storage in regions characterised by a low flux of magma into the lithosphere, relative to volcanic centres located above the centre of mantle plumes with a large buoyancy flux (and thus generating a large flux of magma). The flux of mantle-derived magma into the lithosphere is important because it is thought to impart a first-order control on the development of large silicic magma bodies (Barker et al., 2020) and the homogeneity of erupted

55   liquids (Geist et al., 2014). Furthermore, placing constraints on the physicochemical characteristics of

56   magma storage at low melt flux ocean island volcanoes is essential for determining the influence of

57   mantle dynamics and melt generation processes on the structure and physical characteristics of sub-

58   volcanic magma plumbing systems. In the absence of detailed monitoring data, petrological and

59   geochemical analyses of volcanic products from past eruptions represent the only available tools for

60   determining the structure and processes operating within these systems.

61   Isla Floreana in the south-eastern Galápagos Archipelago is currently located ~100 km downstream

62   from where the Galápagos plume impacts on the base of the lithosphere beneath the island of Isabela

63   in the western archipelago (Fig. 1; Villagómez et al., 2014). Hence, although the Galápagos plume has

64   a relatively high buoyancy flux (compared to regions such as the Canary Islands; Jackson et al.,

65   2017), Floreana's location relative to the main zone of mantle plume upwelling results in an

66   extremely low flux of magma entering the lithosphere and, consequently, very infrequent volcanic

67   activity (Harpp et al., 2014a; Harpp and Geist, 2018). In this paper, we present a thorough petrological

68   study of scoria, lava and xenolith samples from Floreana and place constraints of the structure, depth

69   and crystallinity of magmatic systems beneath this low melt flux ocean island volcano. We compare

70   our results with more frequently active volcanic centres in the western Galápagos (near the centre of

71   plume upwelling; Geist et al., 1998; Naumann and Geist, 1999; Stock et al., 2018), as well as Iceland

72   and Hawaii (Hammer et al., 2016; Hartley et al., 2018; Poland et al., 2015), to investigate how the

73   flux of magma into the lithosphere influences the depth and crystallinity of sub-volcanic magma

74   storage regions.

2   GEOLOGICAL BACKGROUND

76   The Galápagos Archipelago in the eastern equatorial Pacific is one of the most volcanically active

77   regions on Earth, with eruptions typically occurring every 2–3 years (Global Volcanism Program,

78   2013). Although most historic Galápagos eruptions have taken place on the two westernmost islands

79   of Isabela and Fernandina (Fig. 1), infrequent volcanic activity has also occurred on several islands in

80   the eastern and southern Galápagos (e.g. Santiago in 1906 and Marchena in 1991; Global Volcanism

81   Program, 2013).

82   Volcanoes in the western Galápagos likely emerged within the last 500 kyr (Naumann and Geist,

83   2000), whereas those in the eastern and south-eastern Galápagos are considerably older (eruption ages

84   up to 2.3 Ma and 3.2 Ma have been measured on San Cristobal and Espanola, respectively; Bailey,

85   1976; Geist et al., 1986). In addition, substantial differences in geomorphology and the style of

86   volcanic activity are observed across the archipelago (Geist et al., 1995; Harpp et al., 2014a; Harpp

87   and Geist, 2018). For example, volcanoes in the western archipelago are typified by large summit

88   calderas (<700m deep), which are not present on the eastern islands (Chadwick and Howard, 1991;

89   Cleary et al., 2020; Harpp and Geist, 2018).

90   Geochemical distinctions between the western and eastern/southern Galápagos islands are also

91   observed, which are primarily related to variations in the composition of the underlying mantle source

92   (Geist et al., 1988; Gibson and Geist, 2010; Gleeson et al., 2020; Harpp and White, 2001; White et al.,

93   1993) or the volume flux of mantle-derived magma that ascends into the lithosphere (Geist et al.,

94   1995, 2014; Gibson et al., 2016; Harpp and Geist, 2018). For example, variations in the flux of mantle

95   derived magma are hypothesised to influence the geochemical heterogeneity of erupted basalts at each

96   island: volcanoes in the western archipelago typically erupt a very narrow range of basaltic

97   compositions over hundreds of millennia during their main shield building phase, whereas basalts

98   erupted from a single island in the eastern and/or south-eastern archipelago, such as Floreana, tend to

99   display far greater compositional heterogeneity (Geist et al., 2014; Harpp and Geist, 2018).

100   Floreana is characterised by numerous scoria cones (up to ~600m elevation at Cerro Pajas) and

101   blocky, heavily vegetated lava flows that can typically be traced to the cone from which they

102   originated (Harpp et al., 2014a). The crustal thickness beneath Floreana is ~16 km, similar to that

103   observed in the western Galápagos 10–18 km (Feighner and Richards, 1994), and the lithospheric

104   thickness beneath the western and south-eastern Galápagos is very similar (~50–60 km; Gibson and

105   Geist, 2010). However, recent work has shown that the volumetric eruption rate on Floreana is 1–10

106   $m^3 \cdot yr^{-1}$ over the past 1–1.5 Myrs, millions of times lower than the current effusion rate at volcanoes in

107   the western Galápagos (cf. ~4.4·10^6 $m^3·yr^{-1}$ at Fernandina; Harpp et al., 2014a; Kurz et al., 2014).

108   This variation in volumetric eruption rate likely reflects a substantially lower flux of magma into the

109   lithosphere beneath Floreana than beneath each volcanic centre in the western Galápagos.

110   Additionally, Floreana has a high proportion of pyroclastic deposits compared to the other Galápagos

111   islands (Harpp et al., 2014a) and eruption deposits typically contain a large number of cumulate

112   xenoliths (Lyons et al., 2007). The abundance of pyroclastic deposits and xenoliths on Floreana has

113   been interpreted as evidence for very high magma ascent rates (Harpp et al., 2014a).

114   Floreana is one of the only Galápagos islands that displays evidence for multiple stages in its volcanic

115   evolution. Submarine parts of the island have isotopic and trace element characteristics that are

116   similar to recent basalts erupted on southern Isabela (e.g. Sierra Negra and Cerro Azul, Fig. 1A),

117   whereas the subaerial material is isotopically distinct (high $^{206}Pb/^{204}Pb$ ratios; Harpp et al., 2014). The

118   trace element and isotopic variation in the erupted basalts is mirrored in xenoliths found in the

119   Floreana lava and scoria deposits: gabbroic xenoliths have radiogenic isotope ratios that are similar to

120   modern Isabela basalts, whereas wehrlitic xenoliths have trace element and isotopic compositions that

121   resemble recent Floreana subaerial basalts (Lyons et al., 2007). Variations in the isotopic

122   characteristics of the Floreana lavas (submarine vs subaerial) and xenoliths (gabbros vs wehrlites) are

123   thought to indicate a change in the mean composition of magma produced by mantle melting beneath

124   the island at ~1–1.5 Ma (Harpp et al., 2014a). In this study, we focus on constraining the depth and

125   physical characteristics of magma storage during the most recent period of volcanic activity on Isla

126   Floreana (<1–1.5 Ma) using chemical and textural analysis of crystal phases in lava flows and

127   xenolithic nodules.

3   SAMPLES AND PETROGRAPHY

129   The Floreana samples analysed in this study were collected during a field campaign to the northern

130   part of the island in June 2017 and consist of lavas (27 samples), scoria (2 samples) and xenoliths (4

131   wehrlite, 3 dunite and 2 gabbro samples; Fig. 1B). Most lava samples were collected from the

132   unaltered, low vesicularity cores of blocky flows or glassy flow fronts. The scoria samples were

133   collected from two separate deposits and comprise rapidly cooled tephra fragments (~0.5–2 cm

134   across; 17MMSG16) and scoria bombs (~10 cm across; 17MMSG20). Xenolithic fragments (3–15cm

135   across) were sampled from two different scoria cones on the north-east coast of Floreana and are also

136   found within most lava flows across the entire island (Fig. 1).

3.1   Lavas and scoria

138   The lava and scoria samples analysed in this study are typically olivine phyric with minor andehral

139   clinopyroxene and very rare orthopyroxene. Except for small plagioclase laths in the microcrystalline

140   groundmass, plagioclase crystals are extremely rare in Floreana lavas. Plagioclase macrocrysts are

141   only present in one of our lava samples (17MMSG29) where they occur as isolated phenocrysts and in

142   plagioclase-olivine crystal clots (Table S.1). Abundant olivine and the absence of plagioclase in the

143   Floreana lavas and scoria contrasts with basalts in the central, northern, and western parts of the

144   Galápagos Archipelago, where plagioclase-phyric and ultraphyric basalts are common (Geist et al.,

145   2002; Gibson et al., 2012; Harpp et al., 2014b).

146   Despite their relatively simple mineralogy, Floreana lava and scoria samples contain texturally diverse

147   olivine crystals which can be divided into five distinct groups (Fig. 2):

148   -   Group 1 olivines are present in all lava and scoria samples and are the most abundant type of

149   olivine found in the Floreana basalts (~60-70% of all crystals). They are characterised by

150   homogeneous cores and narrow normally zoned rims (Fig. 2A). Group 1 olivines are

151   generally subhedral to euhedral.

152   -   Group 2 olivines are the second most abundant group in the Floreana lava and scoria deposits

153   (~20-30%) and display reverse zoning patterns. They are typically euhedral, with occasional

154   small embayments (Fig. 2B).

155   -   Group 3 olivines are also reversely zoned, but are distinguished by skeletal overgrowths,

156   indicating significant undercooling of the host magma and rapid crystal growth (Fig. 2C;

157   Donaldson, 1976; Welsch et al., 2014). Group 3 olivines are less abundant than Groups 1 and

158   2 olivines in Floreana lava and scoria deposits (<10%).

159   -   Group 4 olivines are present in low abundance in the Floreana lava and scoria deposits

160   (<10%). They have homogeneous cores and reverse-zoned rims (up to ~300 µm thick). The

161   rims have sieve textures, indicating resorption and chemical disequilibrium with their carrier

162   melts (Fig. 2D).

163   -   Group 5 olivines are only found in a minority of samples and are characterised by the

164   presence of 4 compositional zones with alternating high and low forsterite contents (visible in

165   back-scattered electron images; Fig. 2E and F).

3.2   Xenoliths

3.2.1   *Gabbroic xenoliths*

168 Floreana gabbroic xenoliths predominantly comprise plagioclase (33–66 vol.%), clinopyroxene (28–

169 46 vol.%) and orthopyroxene (5–15 vol.%), with little or no olivine (Table S.2). Plagioclase and

170 pyroxene crystals are typically >500 µm and grain sizes are relatively constant within a single

171 xenolith sample. Where three plagioclase grains meet at a triple junction, 120º grain boundaries

172 indicate a high degree of textural equilibrium (Fig. 3A; Holness et al., 2005). Some of the gabbros

173 display clear clinopyroxene-rich and plagioclase-rich layers (2–5 mm), whereas others have a more

174 irregular mineral distribution.

3.2.2   *Dunitic xenoliths*

176 Cumulus olivine dominates dunitic Floreana xenoliths (>90 vol.%). The olivine crystals are subhedral

177 to euhedral and may have undergone partial textural re-equilibration, with some olivine triple

178 junctions approaching 120º grain boundaries. Minor intercumulus clinopyroxene is present along

179 grain boundaries and between pre-existing olivine crystals (Fig. 3B).

3.2.3   *Wehrlitic xenoliths*

181 Floreana wehrlitic xenoliths contain olivine (>50 vol.%), clinopyroxene (20–40 vol.%),

182 orthopyroxene (~0–7 vol.%) and minor spinel (<1 vol.%; Table S.1). Clinopyroxene typically occurs

183 as large (<5 mm) oikocrysts, which enclose rounded olivine chadacrysts (<500 µm in diameter and

184 separated by distances of <400 µm; Fig. 2C and D). In the most pyroxene-rich samples (e.g.

185 17MMSG03a), clinopyroxene crystals contain fine-scale orthopyroxene exsolution lamallae (Fig. 2E

186 and F). Olivine grains that are not enclosed by clinopyroxene are typically larger (>1 mm) and more

187 euhedral than the chadacrysts. In some samples, the boundary between clinopyroxene and olivine

188 crystals is characterised by a thin (<20-30 μm) layer of glass and very fine-grained microcrysts.

189 Orthopyroxene is an intercumulus phase in the wehrlitic xenoliths and has an anhedral morphology,

190 infilling the space between earlier formed clinopyroxene and olivine grains. Our observations of

191 dunitic and wehrlitic xenoliths (which have the isotopic signatures of modern day Floreana basalts;

192 Lyons et al., 2007) indicate that the typical order of crystallisation beneath Floreana is olivine,

193 followed by clinopyroxene, with little to no crystallisation of plagioclase.

4 ANALYTICAL METHODOLOGY

4.1 Electron microprobe analysis

196 Glass chips, olivine and clinopyroxene crystals were hand-picked from crushed scoria and lava

197 samples, mounted in epoxy or indium, and then ground and polished prior to analysis (crystals

198 mounted in indium were polished individually prior to mounting). Xenolithic crystals were analysed

199 as individual crystals mounted in indium or *in situ* in petrographic thin sections. The major and minor

200 element concentrations of olivine, clinopyroxene and glass were measured using a Cameca SX100

201 electron microprobe in the Department of Earth Sciences, University of Cambridge. Calibrations were

202 made using mineral and metal standards prior to each analytical session (see Gleeson and Gibson,

203 2019 for details). Glasses in the two Floreana scoria samples were analysed using a 6 nA, 15 kV,

204 defocused (5 μm) beam for most elements. Na and K were analysed first (10 s peak count time) to

205 avoid alkali migration. Other elements were analysed with peak count times of 10 s (Si), 20 s (Fe), 30

206 s (Al, P, Ca, Mg), 40 s (Mn), or 60 s (Ti). Sulphur was analysed last using a 20 nA beam current and a

207 60 s peak count time.

208 Pyroxene compositions were determined by spot analyses using a 20 nA, 15 kV, focused (~1 μm)

209 beam, with Na, K and Si analysed first (10 s). Element maps of Cr, Ti, and Al in key clinopyroxene

210 crystals from the Floreana xenoliths were created using a 60 nA, 15 kV, focused (~1 μm) beam, with

211 a dwell time of 150 ms. Cr counts were collected on a PET and a LIF crystal, Al counts were

212   collected on two TAP crystals, and Ti counts were collected on a PET crystal. Olivine electron

213   microprobe analysis was carried out using the method outlined in Gleeson and Gibson (2019).

214   Analytical uncertainties were tracked through analysis of appropriate Smithsonian Microbeam

215   Standards (Jarosewich et al., 1980). Accuracy is typically between 98 and 102% for all phases. 2σ

216   analytical precision of clinopyroxene and olivine analysis is typically better than 2–3% for major

217   elements (>1 wt%) and typically ~5-10% for minor elements (<1 wt%). Similarly, the 2σ precision for

218   glass analysis is typically <3% for major elements, ~5% for Na, and ~10% for K (See Supplementary

219   File).

4.2   Laser ablation Inductively Coupled Plasma Mass Spectrometry

221   Trace element concentrations were measured in the apparent cores (i.e. as exposed in the 2D plane) of

222   clinopyroxene crystals from scoria and xenolith samples using an ESI193 laser coupled to a Nexion

223   350D inductively coupled plasma mass spectrometer in the Department of Earth Sciences, University

224   of Cambridge. Analyses were collected in spot mode using a 20 Hz laser repetition rate, 4 J/cm^2

225   fluence and 80 μm spot size, or in transect mode using a 10 Hz repetition rate, 3.5 J/cm^2 fluence and

226   30 μm spot size. For transects, individual spots were offset into two (alternating) lines to increase the

227   spatial resolution. Laser ablation inductively coupled plasma mass spectrometry (LA-ICP-MS) data

228   reduction was carried out in Iolite$^©$, with NIST 612SRM as the standard reference material and Ca

229   (from electron microprobe analysis) as the internal reference standard. Analytical accuracy was

230   tracked using a USGS glass standard (Jochum et al., 2016) and is between 95% and 105% for most

231   elements (See Supplementary File). 2σ analytical precision of spot analyses was monitored through

232   analysis of an in-house clinopyroxene standard and is 5–10% for the light rare-earth elements

233   (LREE), Y, Sr, and Zr and 10–20% for the heavy rare earth element (HREE). 2σ analytical precision

234   is ~10% for all elements of interest (Ce, Y) in transect analyses.

5 GLASS AND MINERAL CHEMISTRY

5.1 Matrix glass compositions

The matrix glass compositions measured in one scoria (17MMSG16) and one glassy lava sample

(17MMSG12) from Floreana have very similar MgO concentrations (6.06–6.36 wt%) but exhibit

differences in the concentrations of other elements (Fig. 4). For example, sample 17MMSG12 has

consistently lower TiO_2 and Al_2O_3 concentrations than 17MMSG16, which must either reflect

heterogeneity in the composition of primary mantle melts or variations in crustal processing (e.g. the

extent of plagioclase or clinopyroxene crystallisation; Fig. 4). Differences between our matrix glass

major element analyses and previously-published whole-rock data from Floreana (Harpp et al., 2014a)

are primarily due to olivine accumulation in the whole-rock samples (additional accumulation of

clinopyroxene may explain the high CaO content of some whole-rock samples; Fig. 4C).

Our Floreana matrix glass analyses have higher Al_2O_3 concentrations than basaltic glass and whole-

rock measurements from the western Galápagos Archipelago (excluding whole-rock samples with

accumulated plagioclase, Fig. 4D; Geist et al., 2002). This indicates substantially lower extents of

plagioclase fractionation in the Floreana magmatic system and is consistent with the scarcity of

plagioclase phenocrysts in erupted Floreana lavas. Reduced plagioclase crystallisation could be due to

the major element composition or H_2O content of primary mantle melts and/or the increased pressure

of magma storage (Asimow and Langmuir, 2003; Neave et al., 2019; Thompson, 1987; Winpenny and

Maclennan, 2011).

5.2 Olivine compositions

Olivine crystals in our Floreana lava and scoria samples show large variations in their forsterite

contents (Fo = 70–92, where Fo=(Mg/(Mg+Fe^{2+}) molar) with histograms showing a primary density

peak at Fo~85 (Fig. 5), more primitive than the olivine composition in equilibrium with basaltic

glasses from Floreana (K_D = 0.30; Roeder and Emslie, 1970). Although there is no clear correlation

between Fo and Ca concentration in these crystals, the most forsteritic olivines (Fo>83) have

260   extremely diverse Ca contents (~250 to ~2600 ppm; Fig. 5), whereas crystals with lower Fo contents

261   (<83) have ubiquitously low Ca concentrations (<1500 ppm). Floreana olivines separated from the

262   lava and scoria samples also have a large range of Ni concentrations (~700 to ~3200 ppm), consistent

263   with crystallisation from a peridotite-derived melt (Fig. 5; Gleeson and Gibson, 2019; Herzberg,

264   2011; Matzen et al., 2017b, 2017a). All olivine crystals analysed in the wehrlite and dunite xenoliths

265   have a narrow range of Fo contents (83-87) and, crucially, have uniformly low Ca concentrations

266   (<1000 ppm) and moderately high Ni contents (~2000 ppm). The range in Ca contents contrasts with

267   olivines from other Galápagos islands where Ca is typically >1000 ppm (Gleeson and Gibson, 2019;

268   Vidito et al., 2013). The Ca and Ni contents of our Floreana olivines are inversely related at a set Fo

269   content (Fig. 5).

270 5.3   Clinopyroxene compositions

271   *5.3.1   Major elements*

272   The Floreana clinopyroxenes analysed in this study (from scoria and xenolith samples) are augites

273   ($En_{~48.5}Fs_{~8}Wo_{~43.5}$) and have a relatively high Mg# (0.85–0.90; Mg# = Mg/(Mg+Fe$_t$) molar). The

274   clinopyroxenes typically contain very high Na concentrations (<1.58 wt% Na$_2$O, <0.11 Na atoms per

275   formula unit; Fig. 6A) and, correspondingly, up to 10% of the jadeite component. In general,

276   clinopyroxene separates from scoria samples display a wide range of Na concentrations, whereas the

277   xenolithic clinopyroxenes have high Na contents (Fig. 6A). The Floreana clinopyroxenes display a

278   large range of Cr contents, ranging from <0.05 wt% in the most evolved crystals to ~1.72 wt% in the

279   more primitive crystals (Fig. 6B).

280   *5.3.2   Trace elements*

281   Our Floreana clinopyroxenes display a wide range of geochemical enrichment, with LREE to MREE

282   ratios varying from [La/Sm]$_n$ ~0.2 to [La/Sm]$_n$ ~3.1. Xenolithic clinopyroxenes typically have more

283   enriched trace element ratios (such as [La/Sm]$_n$ or [Ce/Y]$_n$) than clinopyroxenes from the scoria

284   samples (Fig. 7). Furthermore, the melt [La/Sm]$_n$ ratios calculated to be in equilibrium with

285   clinopyroxenes from the scoria and xenolith samples range from ~1 to ~15 (calculated using the

286 elastic strain model of Wood and Blundy (1997) at 1225ºC and 700 MPa; Fig. 7B), significantly

287 greater than the range measured in Floreana whole-rock samples (~2–5, with a small number of

288 outliers up to ~7.5; Harpp et al. 2014a). Almost all of the xenolithic crystals, and a large proportion of

289 the clinopyroxenes separated from scoria deposits, are too enriched to be in equilibrium with the

290 typical composition of melts erupted on Floreana (Harpp et al.,2014a). In addition, there is a strong

291 correlation between the Na concentrations and highly/moderately incompatible trace element ratios of

292 the Floreana clinopyroxenes, such that crystal with high incompatible trace element concentrations

293 typically contain a high jadeite component (Fig. 7A).

6 MAGMA SYSTEM ARCHITECTURE BENEATH ISLA FLOREANA

294
295

6.1 Mush crystallisation and textural equilibration

297 Based on pyroxene trace element and radiogenic isotope ratios, Lyons et al. (2007) hypothesised that

298 gabbroic xenoliths in the Floreana lava and scoria deposits formed in an ancient (>1-1.5 Ma)

299 magmatic system, compositionally similar to those currently beneath Cerro Azul and Sierra Negra

300 volcanoes in the western Galápagos Archipelago. In contrast, wehrlite xenoliths preserve isotopic

301 ratios similar to more recent subaerial lavas on Floreana, suggesting that they are fragments of the

302 present-day magmatic system (Lyons et al., 2007).

303 Our wehrlitic xenoliths preserve an original igneous texture (clinopyroxene oikocrysts surrounding

304 olivine chadacrysts; Wager et al., 1960) and display no evidence of textural re-equilibration (e.g. 120º

305 dihedral angles) or metamorphic breakdown of plagioclase (e.g. pseudomorphs or relict cores; Lyons

306 et al., 2007). The presence of orthopyroxene lamellae in some clinopyroxenes indicates that they

307 cooled relatively slowly (Poldervaart and Hess, 1951). Hence, we suggest that the clinopyroxene

308 crystals in our wehrlitic xenoliths grew within an olivine-dominated cumulate mush (i.e. interstitial

309 growth of clinopyroxene oikocrysts; Wager et al., 1960). The rounded morphology and small size of

310 olivine chadacrysts, relative to olivine crystals that are not enclosed by clinopyroxene oikocrysts (Fig.

311 3D), indicates that clinopyroxene growth may have been at the expense of olivine (e.g. Lissenberg

312   and MacLeod, 2016). If clinopyroxene growth is principally within a crystal-rich (i.e. relatively

313   viscous and immobile) mush zone, this could explain its relatively low abundance in Floreana lava

314   and scoria deposits (<5% of separated crystals).

315   In contrast with the wehrlites, three-grain plagioclase triple junctions in our gabbroic xenoliths have

316   ~120° dihedral angles (Fig. 3A), indicating a high degree of textural equilibration (Holness et al.,

317   2019, 2005). Plagioclase textural equilibrium, along with the two-pyroxene phase assemblage,

318   suggests that the gabbroic xenoliths represent magmatic cumulates which were stored at high

319   temperatures (>900°C) on long timescales (Holness et al., 2006). These petrographic observations are

320   consistent with the gabbroic nodules sampling an ancient magmatic system beneath Floreana (>1 Ma;

321   Lyons et al., 2007).

6.2   Mush disaggregation prior to eruption

322

6.2.1   *Insights from olivine compositional heterogeneity*
323

324   Olivine crystals separated from the Floreana lava and scoria samples have a wide range of zoning

325   patterns, morphologies, and compositions (Fig. 2). The five olivine groups identified in the Floreana

326   samples have distinct morphologies and zoning patterns (see Section 2 above), suggesting chemically

327   heterogeneous magma storage (Holness et al., 2019). In particular, the most evolved crystals (Group

328   4; Fo~70–75) are in equilibrium with melts that are more evolved than the Floreana erupted basalts.

329   This is consistent with a recent study which identified highly evolved (rhyolitic) magmas beneath

330   basaltic volcanoes in the western Galápagos Archipelago (Stock et al., *in review*).

331   As Fe-Mg interdiffusion in olivine is geologically fast (Costa et al., 2020), preservation of forsterite

332   zoning in the Floreana olivine crystals suggests that multiple magma batches interacted on relatively

333   short pre-eruptive timescales. In Group 5 olivines, for example, four compositional zones are

334   preserved over ~100-200 μm near the rim (Fig. 2E and F). Whilst we do not have enough Group 5

335   olivine crystals to calculate statistically robust timescales of pre-eruptive magma interactions using

336   diffusion chronometry, complex forsterite zoning over ~100 μm is estimated to last <3 yrs at the

337   approximate temperature of basaltic magma storage (~1225°C; using diffusion coefficients from

338   Chakraborty, 2010). Therefore, we suggest that the range of crystal morphologies and major element

339   compositions displayed by the Floreana olivines in lava and scoria deposits indicates mixing and

340   amalgamation of chemically heterogeneous magma storage regions over relatively short timescales

341   prior to eruption.

342   The minor element chemistry of the olivine crystals allows us to investigate the crystallinity of these

343   chemically diverse magma storage regions. Olivine crystals in our Floreana lava and scoria deposits

344   have an unusually low, and large range of Ca concentrations (~250–2600 ppm compared with ~1500-

345   3000 in the eastern Galápagos; Gleeson and Gibson, 2019; Fig. 5A). The lower end of the range in Ca

346   concentrations measured in the Floreana lava and scoria deposits overlaps with those observed in

347   cumulate xenoliths (wehrlites) and thus are unlikely to represent mantle olivines (Thompson and

348   Gibson, 2000). Previous studies have shown that the Ca concentration of magmatic olivine is sensitive

349   to several parameters, including: (i) the temperature of the system (Adams and Bishop, 1982; Köhler

350   and Brey, 1990; Shejwalkar and Coogan, 2013); (ii) the H_2O content of the co-existing melt phase

351   (Gavrilenko et al., 2016); and (iii) the major element composition of the co-existing melt phase

352   (Herzberg, 2011). However, the diversity of Ca concentrations in our Floreana olivines is too large to

353   be caused by variations in T alone (assuming that the difference between the crystallisation

354   temperature and final storage temperature is <300°C; see Section 6.4). In addition, H_2O contents of ~3

355   wt% would be required to explain the lowest Ca concentrations in the Floreana olivines (according to

356   the hygrometer of Gavrilenko et al., 2016), which is far in excess of that measure in Floreana

357   submarine glasses by Peterson et al. (2017). Hence, Ca variations in Floreana olivines likely result

358   from compositional variability in the co-existing melt phase.

359   Although olivine Ca variations are often interpreted to reflect lithological heterogeneity of the mantle

360   source (resulting in primary melt compositional variability), this is inconsistent with the Ni contents

361   of olivine crystals from Floreana (Fig. 5B; Gleeson and Gibson, 2019). An alternative process is

362   therefore required to explain the variability of olivine Ca concentrations and, specifically, the

363   presence of olivine crystals with <1000 ppm Ca. This process must reduce the Ca concentration of the

364   melt phase (and co-existing olivines), without simultaneously reducing the melt Mg# (as low Ca

365   concentrations are observed across the entire range of forsterite contents in the Floreana olivines; Fig.

366   5A) and may be accompanied by slight variations in *T* or melt H_2O concentration.

367   Evidence for the origin of the low-Ca olivines in the lava and scoria deposits is present in texture and

368   composition of the wehrlitic xenoliths, which contain uniformly low-Ca olivine crystals (<1000 ppm;

369   Fig. 5A). The petrography of the wehrlitic xenoliths attests to clinopyroxene growth within olivine-

370   dominated mush regions. Clinopyroxene crystallisation within this mush would extract CaO and MgO

371   from the residual melt. However, in an olivine-rich mush, the large reservoir of MgO contained within

372   the cumulus olivine grains would buffer the residual melt at a near-constant Mg# during

373   clinopyroxene crystallisation (Meyer et al., 1989). In contrast, the CaO concentration of the melt is

374   not buffered and decreasing melt CaO contents, due to clinopyroxene crystallisation, will cause the

375   CaO concentration of cumulus olivine grains to decrease (as a result of diffusive re-equilibration).

376   Intercumulus clinopyroxene growth would also increase the H_2O concentration of the residual melt

377   phase, decreasing the partition coefficient of Ca into olivine (Gavrilenko et al., 2016). Therefore, if

378   these mush-zone crystals are entrained into ascending melts prior to eruption, growth of

379   clinopyroxene within an olivine-dominated mush could explain the presence of anomalously low Ca

380   concentrations in the Floreana olivines separated from lava and scoria deposits.

381   As the majority of olivine analyses from the Floreana lava and scoria deposits have low Ca

382   concentrations (<1000 ppm) that overlap with those in xenolithic nodules, we suggest that a large

383   proportion of the erupted crystal cargo derives from highly crystalline magma storage regions. Higher

384   Ca concentrations (>1500 ppm) are only found in a small number of forsteritic crystals (Fo>83) in the

385   lava and scoria samples (Fig. 5A). As olivine crystals formed from peridotitic melts that have not

386   undergone clinopyroxene growth will typically have Ca concentrations >1500 ppm (Gleeson and

387   Gibson, 2019; Herzberg, 2011), we interpret these crystals to have grown within liquid-rich magma

388   storage regions where magmatic differentiation occurs by fractional crystallisation.

389   However, olivine crystals from the Floreana lava and scoria deposits cannot simply be divided into

390   low Ca (<1000 ppm) and high Ca (>1500 ppm) populations (Fig. 5A). A substantial number of olivine

391   crystals have intermediate compositions (Ca = 1000–1500). We interpret these as being sourced from

392 regions where growth of clinopyroxene was ongoing at the time of mush disaggregation. Thus, the

393 olivine crystal cargo of the Floreana magmas is predominantly derived from crystal-rich domains that

394 vary from highly crystalline (Ca <1000 ppm) to moderately crystalline (Ca = 1000–1500 ppm). Only

395 a small number of olivine crystals preserve compositions consistent with fractional crystallisation in

396 liquid-rich storage regions (Ca >1500 ppm).

397 *6.2.2   Insights from clinopyroxene major element compositions*
398 The compositions of clinopyroxene crystals from the Floreana scoria also overlap with those in our

399 xenolith samples, supporting the hypothesis that some of the erupted crystals are derived from

400 disaggregated sub-volcanic mush. We used hierarchical cluster analysis to subdivide our 567

401 clinopyroxene major element analyses from the Floreana scoria and xenolith samples to determine the

402 proportion of material that is derived from each xenolith lithology in the erupted crystal cargo. We

403 find that our clinopyroxene analyses form three distinct groups (Fig. 8):

404   -   Group 1 clinopyroxenes are predominantly from the wehlite and dunite xenoliths and include

405   90% of our analyses from these samples. 39% of clinopyroxenes analysed from the scoria

406   samples also fall into this group.

407   -   Group 2 clinopyroxenes include all analyses from the gabbroic xenoliths, and ~10% of

408   analyses from crystals separated from the scoria samples.

409   -   Group 3 clinopyroxenes are dominantly analyses from scoria derived clinopyroxenes (~50%

410   of analyses from the scoria separates). However, 10% of analyses from the wehrlite and

411   dunite xenoliths also fall into this group.

412 Of our 248 clinopyroxenes analysed from the Floreana scoria samples, approximately half are

413 classified as Group 3 and thus have major element compositions that do not show any affinity to

414 either the wehrlite/dunite or gabbroic cumulates. Therefore, these crystals may represent autocrysts

415 (with growth in liquid-rich magma storage regions). The remainder of clinopyroxene analyses from

416 the scoria samples are either compositionally analogous to those in the wehrlite and dunite xenoliths

417 (Group 1; 39%) or the gabbroic xenoliths (Group 2; 11%); we interpret these as representing

418 disaggregated sub-volcanic mush or wall rock. The high proportion of the clinopyroxene crystal cargo

419 that is derived from highly crystalline storage regions beneath Floreana is consistent with our

420 interpretation of olivine minor element concentrations.

6.3 Reactive Porous Flow within a cumulate mush

421

422 Whilst the olivine and clinopyroxene major and minor element concentrations show that a large

423 proportion of the erupted crystal cargo is derived from highly crystalline magma storage regions,

424 clinopyroxene trace element concentrations (and zoning) reveal the magmatic processes that operate

425 within these crystal-rich domains. The trace element composition of melts in equilibrium with our

426 clinopyroxene crystals are calculated using the model of Wood and Blundy (1997). The results

427 indicate that many of our clinopyroxene analyses have incompatible trace element ratios (e.g.

428 $[Ce/Y]_n$) which are more enriched than any erupted basalt from Floreana (Harpp et al., 2014a). In fact,

429 nearly all clinopyroxenes analyses from our xenolith samples, and ~50% of clinopyroxene analyses

430 from the scoria samples, record trace element disequilibrium with the typical trace element

431 composition of the Floreana basalts (Fig. 7 and 9). Over-enriched equilibrium melt signatures are

432 characteristics of Group 1 clinopyroxenes (i.e. chemical affinity to the wehrlitic or dunitic xenoliths),

433 whereas crystals that are near trace element equilibrium with Floreana basalts typically have Group 3

434 major element compositions (i.e. the autocryst group).

435 Petrographic observations and olivine minor element data indicate that the Floreana sub-volcanic

436 system is characterised by clinopyroxene crystallisation within an olivine-dominated mush. If the

437 clinopyroxene grew from trapped melt within an olivine-dominated mush, progressive crystallisation

438 would increase the concentration of highly incompatible trace elements (e.g. Ba, La, Ce) relative to

439 less incompatible trace-elements (e.g. Sm, Y) in the residual melt. A simple fractional crystallisation

440 model indicates that ~80% crystallisation is required to generate melt $[Ce/Y]_n$ ratios that are in

441 equilibrium with enriched clinopyroxenes from the scoria samples and even greater extents of

442 crystallisation (~90%) would be required to generate the extremely high $[Ce/Y]_n$ ratios in some of the

443 xenolithic clinopyroxenes (Fig. 9). Such extensive crystallisation would be expected to result in the

444 saturation and crystallisation of plagioclase and other accessory phases (e.g. apatite,

445   magnetite/ilmenite, quartz), which are observed in more evolved xenoliths from Rabida island in the

446   central Galápagos (Holness et al., 2019). However, these phases are absent in the Floreana xenoliths,

447   indicating that another process is responsible for generating the anomalous trace element signatures of

448   the melts in equilibrium with our clinopyroxenes.

449   One possible mechanism for generating the observed trace element over-enrichment is reactive porous

450   flow, where clinopyroxene saturated melts ascend through highly-crystalline magmatic systems

451   causing dissolution of the existing crystal framework and precipitation of clinopyroxene (Lissenberg

452   and MacLeod, 2016). Reactive porous flow can result in net replacement of olivine by clinopyroxene,

453   leading to enrichment of highly- to moderately-incompatible trace elements in the resulting melt and

454   co-existing crystal phases (Coogan et al., 2000; Gao et al., 2007; Lissenberg et al., 2013; Lissenberg

455   and MacLeod, 2016), and is consistent with the petrography of the Floreana xenoliths. For example,

456   major element maps of clinopyroxene crystals in the Floreana wehrlites show that they are zoned,

457   with Ti-rich rims (Fig. 10); equivalent zoning patterns have been attributed to reactive porous flow in

458   plutonic clinopyroxenes from the oceanic crust (e.g. Hess Deep; Lissenberg and MacLeod, 2016).

459   Furthermore, reactive porous flow is consistent with the small size and rounded morphology of

460   olivine chadacrysts. In addition, if pre-existing Cr-spinel was dissolved by the reacting melt, then

461   reactive porous flow could also explain the high Cr contents of clinopyroxene in our wehrlitic

462   xenoliths (Fig. 6; Lissenberg and MacLeod, 2016).

463   To test whether reactive porous flow of clinopyroxene saturated melts through an olivine-dominated

464   mush is consistent with the trace element compositions of melts calculated to be in equilibrium with

465   our Floreana clinopyroxenes, we use the zone refining model of Harris (1957; Fig. 9):

466
$$\frac{C_l}{C_l^o} = \frac{1}{D} - (\frac{1}{D} - 1)^{-DI}$$

467   (eq. 1)

468   where D is the bulk partition coefficient; C_l^o and C_l are the initial and final concentration of that

469   element in the melt phase, respectively; and I is the 'equivalent volumes of solid processed by the

470   liquid' (Lissenberg and MacLeod, 2016). The model assumes that a migrating melt front depletes solid

471   phases of their incompatible trace elements owing to partial melting, and has previously been

472   employed to investigate geochemical signatures in oceanic gabbros (Lissenberg and MacLeod, 2016).

473   The model produces melts with trace element compositions that are comparable with those in

474   equilibrium with our Floreana clinopyroxenes (i.e. $[Ce/Y]_n$ ~8-13) using I values similar to that

475   invoked in other magmatic settings worldwide (~4–10; Lissenberg and MacLeod, 2016). Hence,

476   reactive porous flow represents a realistic mechanism for generating the geochemical diversity of

477   Floreana clinopyroxenes, including the trace element enriched crystals analysed in the wehrlitic

478   nodules (Fig. 9).

479   In addition, detailed LA-ICP-MS transects of two clinopyroxene grains from the most enriched

480   wehrlitic xenolith analysed in this study (17MMSG02c) show clear trace element zoning (Fig. 11).

481   The core of the larger clinopyroxene crystal has low $[Ce]$ and $[Ce/Y]_n$ contents that are approximately

482   in equilibrium with Floreana basalts (Harpp et al. 2014a; Fig. 11a), whereas the mantle is

483   characterised by increasing $[Ce]$ and $[Ce/Y]_n$ contents towards the rim. We interpret this as core

484   crystallisation from a melt with a trace element signature similar to that of erupted Floreana basalts

485   (Harpp et al., 2014a), followed by growth from a melt which became progressively enriched during

486   reactive porous flow (Fig. 11).

487   The mantle of the second, smaller xenolithic clinopyroxene shows a similar rim-ward increase in $[Ce]$

488   (interpreted as progressive melt enrichment during reactive porous flow). However, the $[Ce]$ and

489    $[Ce/Y]_n$ values of the crystal core are too high to be in equilibrium with erupted Floreana basalts (Fig.

490   11C). This is consistent with spot analyses of clinopyroxene cores in other crystals analysed in this

491   study. The high $[Ce]$ and $[Ce/Y]_n$ values in crystal cores cannot be explained by inward diffusion of

492   Ce, owing to significant differences in the diffusivities of Ce and Y and similar $[Ce]$ and $[Y]$ zoning

493   patterns in our two crystal transects (Fig. 11; Van Orman, 2001). Instead, we suggest that the high

494   apparent core $[Ce]$ and $[Ce/Y]_n$ contents in many of the Floreana clinopyroxenes record crystallisation

495   from melts that had already undergone geochemical enrichment via reactive porous flow. However,

496   we cannot discount that our apparent clinopyroxene cores are fragments of larger oikocrysts that have

497 been broken during mush disaggregation or sample crushing and, as a result, do not represent the true

498 core compositions of each crystal.

499 Nevertheless, our clinopyroxene major and trace element data, as well as petrographic observations of

500 the wehrlitic xenoliths, provide substantial evidence that reactive porous flow is an important

501 mechanism of melt migration and melt differentiation in highly crystalline magma storage regions

502 beneath Floreana. Although reactive porous flow has been identified as an important process in MOR

503 gabbros, this is the first study to identify reactive porous flow in an ocean island setting.

6.4 Petrographic estimates of magma storage pressures

505 Petrological and geophysical constraints on magma storage depths exist for several recently active

506 volcanoes in the western Galápagos Archipelago (Bagnardi et al., 2013; Case et al., 1973; Geist et al.,

507 1998; Stock et al., 2018; Vigouroux et al., 2008). However, in the absence of geophysical data (owing

508 to a paucity of recent eruptions), there are far fewer constraints on the structure of magma storage

509 regions in the eastern and south-eastern archipelago. To date, the only investigation of magma storage

510 depths beneath these volcanoes is by Geist et al. (1998), who undertook a visual comparison between

511 whole-rock lava compositions and the MORB olivine + plagioclase + augite + melt pseudoinvariant

512 point, parameterised by Grove et al. (1992). This approach is subject to substantial uncertainty, but the

513 authors suggest that Floreana magmas consistently equilibrate at >5 kbar (typically >7 kbar) at a

514 depth >16 km, within the upper mantle.

515 We used three petrological barometers to provide improved constraints on magma storage depths

516 beneath Floreana. First, we applied the clinopyroxene-only barometer of Putirka (2008), in which

517 pressure and temperature are solved iteratively based solely on the clinopyroxene major element

518 composition (primarily the jadeite component; standard error of estimate [SEE] = ±310 MPa).

519 Second, we applied the clinopyroxene-melt barometer of Neave and Putirka (2017), which uses the

520 composition of a co-existing melt phase and the proportion of the Jadeite component in clinopyroxene

521 to calculate the pressure of crystallisation (SEE = ±140 MPa; pressure is solved iteratively with

522 temperature using the clinopyroxene-melt thermometer of Putirka, 2008). Third, for the xenolithic

523   nodules, we estimate the final pressure and temperature of storage using the two-pyroxene

524   thermobarometer of Putirka (2008) (SEE = ±260 MPa).

525   Taken at face value, initial application of the clinopyroxene-only barometer to all clinopyroxene

526   analyses from the scoria and xenolith samples gives a range of pressure estimates between ~450 MPa

527   and ~1800 MPa. However, reactive porous flow has a substantial influence on the compositions of the

528   Group 1 (and Group 2) clinopyroxenes, which may influence the barometric results. Specifically,

529   crystals that show evidence for reactive porous flow also have elevated Na concentrations, leading to

530   an anomalously high jadite component. Therefore, we filter our dataset to remove crystals that show a

531   chemical signature indicative of reactive porous flow and only use Group 3 clinopyroxenes that have

532   trace element compositions in equilibrium with the Floreana basalts (using the whole-rock data from

533   Harpp et al. 2014) in our barometric calculations (n=78). Results indicate that crystallisation beneath

534   Floreana occurs at a pressure of 766 ±322 MPa (2σ of calculated pressures), which equates to a depth

535   of 25.2 ±9.9 km (using the crustal density estimate of Putirka (1997) and a mantle density estimate of

536   3300 km/m^3; Fig. 12).

537   Application of the Neave and Putirka (2017) clinopyroxene-melt barometer requires identification of

538   equilibrium clinopyroxene-liquid pairs. We achieve this using an automated melt-matching algorithm

539   (as in Winpenny and Maclennan, 2011, Neave and Putirka, 2017, Stock et al. 2018), with K_D(Fe-Mg),

540   diopside-hedenbergite, enstatite-ferrosillite and calcium Tschermak's equilibrium tests (K_D(Fe-Mg)

541   within ±0.03 other components within 2 SEE; Putirka, 1999, Putirka, 2008, Mollo et al., 2013). We

542   used the whole-rock data of Harpp et al. (2014a) and basaltic glass analyses from this study as

543   potential equilibrium liquids. Input crystal compositions were again filtered to remove analyses that

544   showed evidence of reactive porous flow (i.e. only Group 3 clinopyroxenes in equilibrium with the

545   Floreana whole-rock were used). In total, 70 of the 78 input clinopyroxene analyses returned at least

546   one equilibrium match to either the basaltic glass or whole-rock compositions. Where clinopyroxene

547   compositions produced an equilibrium match with more than one equilibrium melt, an average melt

548   composition was used in the barometric model. Results from this barometer indicate that magma

549   crystallisation occurred at 717 ±165 MPa (23.7 ±5.1 km) and 1224 ±33°C (Fig. 12).

550   Clinopyroxene-orthopyroxene thermobarometry records the final storage conditions of the cumulate

551   xenoliths, rather than the crystallisation conditions of clinopyroxene autocrysts (orthopyroxene is only

552   found as an intercumulus phase). Temperature and pressure estimates were only calculated from

553   orthopyroxene-clinopyroxene pairs in wehrlite and dunite xenoliths that passed the K_D(Fe-Mg)

554   equilibrium test of Putirka (2008; within ±0.14). Results suggest that the cumulates were stored at

555   ~975–1100ºC and 600–900 MPa, with a mean storage pressure of 712 ±200 MPa (23.7 ±6.4 km; Fig.

556   12).

557   The depths of magma storage calculated from our three petrological barometers show an excellent

558   agreement within the model uncertainties. These new data provide robust evidence that magma

559   storage beneath Floreana occurs below the Moho (~16 km; Feighner and Richards, 1994), in the upper

560   mantle.

7   IMPLICATIONS FOR MAGMATIC PLUMBING SYSTEMS BENEATH LOW MELT FLUX OCEAN ISLAND VOLCANOES

564   Our new petrological and geochemical data show that magma storage beneath Floreana occurs in

565   mush-dominated regions in the upper mantle (Fig. 13). Mineral chemistry (such as low olivine Ca

566   concentrations and clinopyroxene major elements) reveal that a substantial portion of the erupted

567   crystal cargo is derived from disaggregated mush and wall rock material which has been entrained

568   into the ascending magmas. During ascent, magmas may entrain coherent nodules (xenoliths) as well

569   as disaggregated mush (Fig. 13). Coherent nodules represent areas of the magmatic system beneath

570   Floreana that have undergone cooling to temperatures <1100ºC (compared to the clinopyroxene

571   crystallisation temperatures of ~1225ºC) and may represent material from the border of the active

572   mush zone or older, almost completely solidified magma storage regions that are intersected during

573   magma ascent (Fig. 13).

574   Petrographic observations and clinopyroxene trace element chemistry from both the xenolith and

575   scoria samples reveal that clinopyroxene growth occurs via reactive porous flow in the mush-

576   dominated areas beneath Floreana. Reactive porous flow causes distinct trace element enrichment in

577   the percolating melt phase and crystallising clinopyroxene, which can explain the trace element

578   disequilibrium between the erupted Floreana basalts and their clinopyroxene cargo. Nevertheless, the

579   presence of some clinopyroxene crystals with major and trace element compositions in equilibrium

580   with erupted Floreana basalts indicates that at least some crystallisation occurs in liquid-rich sub-

581   volcanic storage regions, likely situated as localised melt pockets within the larger mush zone (Fig.

582   13). Transport of melts modified by reactive porous flow into these melt pockets could impact the

583   LREE enriched signature of the resultant hybridised melts. This could explain the LREE-enriched

584   signature in the Floreana basalts, which is not seen in other regions of the Galápagos Archipelago

585   (Harpp et al., 2014a).

586   Our results indicate substantial differences in the architecture of the magmatic systems beneath

587   Floreana and the frequently active shield volcanoes in the western Galápagos Archipelago. For

588   example, previous petrological and geophysical studies have identified that western Galápagos

589   magmatic systems are characterised by crustal magma storage, often with a large storage region in the

590   mid-to-lower crust (~7 km depth) and a smaller storage region at shallow levels, within the volcanic

591   edifice (~1 km depth; Geist et al. 1998; Bagnardi et al. 2013; Bagnardi and Hooper, 2018; Stock et al.,

592   2018; Fig 12). In contrast, our barometric data indicate that magmas beneath Floreana ascend directly

593   from the upper mantle and undergo no detectable crustal storage. Although mush-rich regions have

594   been inferred beneath the western Galápagos shield volcanoes (based on whole-rock data and the

595   presence of gabbroic glomerocrysts; Chadwick et al., 2011; Geist et al., 1995, 2014; Stock et al.,

596   2018), magmatic differentiation appears to be driven by simple fractional crystallisation and mixing

597   of chemically diverse magmas (Geist et al., 1995; Naumann and Geist, 1999; Stock et al., *in review*).

598   One major factor that differentiates Floreana from shield volcanoes in the western archipelago (on

599   Isabela and Fernandina) is the flux of magma into the lithosphere, as evidenced by variations in the

600   volumetric eruption rate (Harpp et al., 2014a; Harpp and Geist, 2018; Kurz et al., 2014). Hence, we

601   suggest that the greater pressure of magma storage and prevalence of reactive porous flow beneath

602   Floreana, relative to volcanoes in the western archipelago, are related to the substantially lower flux of

603   magma into the lithosphere from the underlying mantle source (and thus the thermal structure of the

604   lithosphere). For example, the magma flux entering the lithosphere beneath Wolf volcano (northern

605   Isabela) has been substantially greater than that beneath Floreana for several 100,000s of years. The

606   high magma flux beneath Wolf maintains the average temperature of the mid-to-lower crust at

607   ~1125°C (ΔT ~22 °C), with only small-scale thermal and compositional heterogeneities present in the

608   sub-volcanic plumbing system (Geist et al., 2014, 2005; Stock et al., 2018, *in review*). In contrast, the

609   flux of magma entering the magmatic system beneath Floreana is much lower and the temperature of

610   the mid-crust is likely to be <<800°C (i.e. significantly cooler than the lowest temperature recorded by

611   the Floreana xenoliths; Fig. 12). As the flux of magma (and heat) from the mantle is insufficient to

612   maintain an elevated crustal geotherm beneath Floreana, magmas that stall in the crust are likely to

613   rapidly crystallise, increase their viscosity, and become uneruptable. Therefore, eruptions must be fed

614   by melts ascending from much deeper storage regions (~700-750 MPa) where super-solidus melts can

615   persist over long time periods.

616   Our results have global implications for the architecture and dynamics of magma storage regions

617   beneath ocean island volcanoes that are characterised by a relatively low flux of magma from the

618   underlying mantle. These include off-axis volcanic systems (e.g. Halekala, Hawaii) and those above

619   low buoyancy flux mantle plumes (e.g. El Hierro, Canary Islands). Figure 14 shows a compilation of

620   published barometric estimates from 'high' and 'low' melt flux systems in some of the most active

621   ocean island systems on Earth (Hawaii, Iceland and Galápagos; Hammer et al., 2016; Hartley et al.,

622   2018; Neave and Putirka, 2017; Poland et al., 2015; Stock et al., 2018). Central volcanic systems from

623   each region typically display relatively low-pressure magma storage compared to regions that are

624   characterised by a comparatively low magma flux from the convecting mantle (i.e. off-axis volcanic

625   systems; Fig. 14). This observation is consistent with the high pressures of magma storage identified

626   at other ocean island volcanoes that are located above mantle plumes with a relatively low buoyancy

627   flux (e.g. >15-25 km at El Hierro in the Canary Islands; Longpre et al., 2014; Taracsák et al., 2019).

628   Hence, we speculate that high-pressure magma storage is characteristic of low melt flux ocean island

629   volcanoes globally.

8 CONCLUSIONS

630

631 Petrographic and geochemical analyses of lava, scoria and xenolith samples from Floreana in the

632 south-eastern Galápagos Archipelago provide new insights into the architecture and dynamics of

633 magma storage beneath low melt flux ocean island volcanoes. Comparison of olivine and

634 clinopyroxene major, minor and trace element contents between our different sample types reveals

635 that a substantial portion of the erupted crystal cargo is derived from mush-dominated magma storage

636 regions beneath Floreana. Mineral textures, highly enriched clinopyroxene trace element signatures

637 and trace element zoning in the xenoliths reveals that reactive porous flow is an important process of

638 chemical differentiation and melt transport within these mush-dominated regions. Mixing between

639 melts that have been geochemically enriched by reactive porous flow and those in overlying liquid-

640 rich storage regions could explain the anomalous LREE enriched signature of the Floreana basalts,

641 which is absent in other parts of the Galápagos Archipelago where reactive porous flow has not been

642 identified.

643 Application of independent petrological barometers to crystals in Floreana scoria and xenolith

644 samples indicates that magmas are stored in the upper mantle (~23.7 ±5.1 km). Floreana is in a distal

645 location to the Galápagos plume where the melt flux entering the lithosphere is low; the depth of

646 magma storage beneath Floreana contrasts with more proximal, higher melt flux volcanoes in the

647 western archipelago where magmas are stored in the crust (Geist et al., 1998; Stock et al., 2018).

648 Comparing our new data with ocean island volcanoes globally (e.g. Hawaii, Iceland and the Canary

649 Islands) reveals that the Galápagos is not unique and that magma storage is ubiquitously shallower in

650 proximal magmatic systems above high buoyancy flux plumes than in off-axis systems, or above low

651 buoyancy flux plumes. We therefore suggest that the flux of mantle-derived magma entering the

652 lithosphere imparts a first-order control on the depth of magma storage beneath ocean island

653 volcanoes.

ACKNOWLEDGEMENTS

654

REFERENCES

663 Adams, G.E., Bishop, F.C., 1982. Experimental investigation of CaMg exchange between olivine,
664   orthopyroxene, and clinopyroxene: potential for geobarometry. Earth Planet. Sci. Lett. 57,
665   241–250. https://doi.org/10.1016/0012-821X(82)90188-1
666 Allan, J.F., Simkin, T., 2000. Fernandina Volcano's evolved, well-mixed basalts: Mineralogical and
667   petrological constraints on the nature of the Galápagos plume. J. Geophys. Res. Solid Earth
668   105, 6017–6041. https://doi.org/10.1029/1999JB900417
669 Amelung, F., Jónsson, S., Zebker, H., Segall, P., 2000. Widespread uplift and 'trapdoor' faulting on
670   Galápagos volcanoes observed with radar interferometry. Nature 407, 993–996.
671   https://doi.org/10.1038/35039604
672 Asimow, P.D., Langmuir, C.H., 2003. The importance of water to oceanic mantle melting regimes.
673   Nature 421, 815–820. https://doi.org/10.1038/nature01429
674 Bagnardi, M., Amelung, F., Poland, M.P., 2013. A new model for the growth of basaltic shields based
675   on deformation of Fernandina volcano, Galápagos Islands. Earth Planet. Sci. Lett. 377–378,
676   358–366. https://doi.org/10.1016/j.epsl.2013.07.016
677 Bailey, K., 1976. Potassium-Argon Ages from the Galápagos Islands. Science 192, 465–467.
678   https://doi.org/10.1126/science.192.4238.465
679 Barker, S.J., Rowe, M.C., Wilson, C.J.N., Gamble, J.A., Rooyakkers, S.M., Wysoczanski, R.J.,
680   Illsley-Kemp, F., Kenworthy, C.C., 2020. What lies beneath? Reconstructing the primitive
681   magmas fueling voluminous silicic volcanism using olivine-hosted melt inclusions.
682 Case, J.E., Ryland, S.L., Simkin, T., Howard, K.A., 1973. Gravitational Evidence for a Low-Density
683   Mass beneath the Galápagos Islands. Science 181, 1040–1042.
684   https://doi.org/10.1126/science.181.4104.1040
685 Chadwick, W.W., Howard, K.A., 1991. The pattern of circumferential and radial eruptive fissures on
686   the volcanoes of Fernandina and Isabela islands, Galápagos. Bull. Volcanol. 53, 259–275.
687   https://doi.org/10.1007/BF00414523
688 Chadwick, W.W., Jónsson, S., Geist, D.J., Poland, M., Johnson, D.J., Batt, S., Harpp, K.S., Ruiz, A.,
689   2011. The May 2005 eruption of Fernandina volcano, Galápagos: The first circumferential
690   dike intrusion observed by GPS and InSAR. Bull. Volcanol. 73, 679–697.
691   https://doi.org/10.1007/s00445-010-0433-0
692 Chakraborty, S., 2010. Diffusion Coefficients in Olivine, Wadsleyite and Ringwoodite. Rev. Mineral.
693   Geochem. 72, 603–639. https://doi.org/10.2138/rmg.2010.72.13
694 Clague, D.A., Denlinger, R.P., 1994. Role of olivine cumulates in destabilizing the flanks of Hawaiian
695   volcanoes. Bull. Volcanol. 56, 425–434. https://doi.org/10.1007/BF00302824
696 Cleary, Z., Schwartz, D.M., Mittelstaedt, E., Harpp, K., 2020. Dynamic Magma Storage at Near-
697   Ridge Hot Spots: Evidence From New Galápagos Gravity Data. Geochem. Geophys.
698   Geosystems 21. https://doi.org/10.1029/2019GC008722
699 Coogan, L.A., Saunders, A.D., Kempton, P.D., Norry, M.J., 2000. Evidence from oceanic gabbros for
700   porous melt migration within a crystal mush beneath the Mid-Atlantic Ridge. Geochem.
701   Geophys. Geosystems 1, n/a-n/a. https://doi.org/10.1029/2000GC000072
702 Costa, F., Shea, T., Ubide, T., 2020. Diffusion chronometry and the timescales of magmatic
703   processes. Nat. Rev. Earth Environ. https://doi.org/10.1038/s43017-020-0038-x
704 Davidge, L., Ebinger, C., Ruiz, M., Tepp, G., Amelung, F., Geist, D., Coté, D., Anzieta, J., 2017.
705   Seismicity patterns during a period of inflation at Sierra Negra volcano, Galápagos Ocean
706   Island Chain. Earth Planet. Sci. Lett. 462, 169–179. https://doi.org/10.1016/j.epsl.2016.12.021

707 Donaldson, C.H., 1976. An experimental investigation of olivine morphology. Contrib. Mineral.
708   Petrol. 57, 187–213. https://doi.org/10.1007/BF00405225
709 Feighner, M.A., Richards, M.A., 1994. Lithospheric structure and compensation mechanisms of the
710   Galápagos Archipelago. J. Geophys. Res. 99, 6711. https://doi.org/10.1029/93JB03360
711 Gao, Y., Hoefs, J., Hellebrand, E., von der Handt, A., Snow, J.E., 2007. Trace element zoning in
712   pyroxenes from ODP Hole 735B gabbros: diffusive exchange or synkinematic crystal
713   fractionation? Contrib. Mineral. Petrol. 153, 429–442. https://doi.org/10.1007/s00410-006-
714   0158-4
715 Gavrilenko, M., Herzberg, C., Vidito, C., Carr, M.J., Tenner, T., Ozerov, A., 2016. A Calcium-in-
716   Olivine Geohygrometer and its Application to Subduction Zone Magmatism. J. Petrol. 57,
717   1811–1832. https://doi.org/10.1093/petrology/egw062
718 Geist, D., Howard, K.A., Larson, P., 1995. The Generation of Oceanic Rhyolites by Crystal
719   Fractionation: the Basalt-Rhyolite Association at Volc n Alcedo, Galápagos Archipelago. J.
720   Petrol. 36, 965–982. https://doi.org/10.1093/petrology/36.4.965
721 Geist, D., Naumann, T., Larson, P., 1998. Evolution of Galápagos Magmas: Mantle and Crustal
722   Fractionation without Assimilation. J. Petrol. 39, 953–971.
723   https://doi.org/10.1093/petroj/39.5.953
724 Geist, D., White, W.M., Albarede, F., Harpp, K., Reynolds, R., Blichert-Toft, J., Kurz, M.D., 2002.
725   Volcanic evolution in the Galápagos: The dissected shield of Volcan Ecuador. Geochem.
726   Geophys. Geosystems 3, 1 of 32–32 32. https://doi.org/10.1029/2002GC000355
727 Geist, D.J., Bergantz, G., Chadwick, W.W., 2014. Galápagos Magma Chambers, in: Harpp, K.S.,
728   Mittelstaedt, E., d'Ozouville, N., Graham, D.W. (Eds.), Geophysical Monograph Series. John
729   Wiley & Sons, Inc, Hoboken, New Jersey, pp. 55–69.
730   https://doi.org/10.1002/9781118852538.ch5
731 Geist, D.J., Fornari, D.J., Kurz, M.D., Harpp, K.S., Adam Soule, S., Perfit, M.R., Koleszar, A.M.,
732   2006. Submarine Fernandina: Magmatism at the leading edge of the Galápagos hot spot.
733   Geochem. Geophys. Geosystems 7, n/a-n/a. https://doi.org/10.1029/2006GC001290
734 Geist, D.J., McBIRNEY, A.R., Duncan, R.A., 1986. Geology and petrogenesis of lavas from San
735   Cristobal Island, Galápagos Archipelago. Geol. Soc. Am. Bull. 97, 555.
736   https://doi.org/10.1130/0016-7606(1986)97<555:GAPOLF>2.0.CO;2
737 Geist, D.J., Naumann, T.R., Standish, J.J., Kurz, M.D., Harpp, K.S., White, W.M., Fornari, D.J.,
738   2005. Wolf Volcano, Galápagos Archipelago: Melting and Magmatic Evolution at the
739   Margins of a Mantle Plume. J. Petrol. 46, 2197–2224.
740   https://doi.org/10.1093/petrology/egi052
741 Geist, D.J., White, W.M., McBirney, A.R., 1988. Plume-asthenosphere mixing beneath the Galápagos
742   archipelago. Nature 333, 657–660. https://doi.org/10.1038/333657a0
743 Gibson, S.A., Dale, C.W., Geist, D.J., Day, J.A., Brügmann, G., Harpp, K.S., 2016. The influence of
744   melt flux and crustal processing on Re–Os isotope systematics of ocean island basalts:
745   Constraints from Galápagos. Earth Planet. Sci. Lett. 449, 345–359.
746   https://doi.org/10.1016/j.epsl.2016.05.021
747 Gibson, S.A., Geist, D., 2010. Geochemical and geophysical estimates of lithospheric thickness
748   variation beneath Galápagos. Earth Planet. Sci. Lett. 300, 275–286.
749   https://doi.org/10.1016/j.epsl.2010.10.002
750 Gibson, S.A., Geist, D.G., Day, J.A., Dale, C.W., 2012. Short wavelength heterogeneity in the
751   Galápagos plume: Evidence from compositionally diverse basalts on Isla Santiago. Geochem.
752   Geophys. Geosystems 13. https://doi.org/10.1029/2012GC004244
753 Gleeson, M.L.M., Gibson, S.A., 2019. Crustal controls on apparent mantle pyroxenite signals in
754   ocean-island basalts. Geology. https://doi.org/10.1130/G45759.1
755 Gleeson, M.L.M., Gibson, S.A., Williams, H.M., 2020. Novel insights from Fe-isotopes into the
756   lithological heterogeneity of Ocean Island Basalts and plume-influenced MORBs. Earth
757   Planet. Sci. Lett. 535, 116114. https://doi.org/10.1016/j.epsl.2020.116114
758 Grove, T.L., Kinzler, R.J., Bryan, W.B., 1992. Fractionation of Mid-Ocean Ridge Basalt (MORB), in:
759   Morgan, J.P., Blackman, D.K., Sinton, J.M. (Eds.), Geophysical Monograph Series. American
760   Geophysical Union, Washington, D. C., pp. 281–310. https://doi.org/10.1029/GM071p0281

761 Hammer, J., Jacob, S., Welsch, B., Hellebrand, E., Sinton, J., 2016. Clinopyroxene in postshield
762   Haleakala ankaramite: 1. Efficacy of thermobarometry. Contrib. Mineral. Petrol. 171, 7.
763   https://doi.org/10.1007/s00410-015-1212-x

764 Harpp, K.S., Geist, D.J., 2018. The Evolution of Galápagos Volcanoes: An Alternative Perspective.
765   Front. Earth Sci. 6. https://doi.org/10.3389/feart.2018.00050

766 Harpp, K.S., Geist, D.J., Koleszar, A.M., Christensen, B., Lyons, J., Sabga, M., Rollins, N., 2014a.
767   The Geology and Geochemistry of Isla Floreana, Galápagos: A Different Type of Late-Stage
768   Ocean Island Volcanism, in: Harpp, K.S., Mittelstaedt, E., d'Ozouville, N., Graham, D.W.
769   (Eds.), Geophysical Monograph Series. John Wiley & Sons, Inc, Hoboken, New Jersey, pp.
770   71–117. https://doi.org/10.1002/9781118852538.ch6

771 Harpp, K.S., White, W.M., 2001. Tracing a mantle plume: Isotopic and trace element variations of
772   Galápagos seamounts. Geochem. Geophys. Geosystems 2, n/a-n/a.
773   https://doi.org/10.1029/2000GC000137

774 Harpp, K.S., Wirth, K.R., Teasdale, R., Blair, S., Reed, L., Barr, J., Pistiner, J., Korich, D., 2014b.
775   Plume-Ridge Interaction in the Galápagos: Perspectives from Wolf, Darwin, and Genovesa
776   Islands, in: Harpp, K.S., Mittelstaedt, E., d'Ozouville, N., Graham, D.W. (Eds.), Geophysical
777   Monograph Series. John Wiley & Sons, Inc, Hoboken, New Jersey, pp. 285–334.
778   https://doi.org/10.1002/9781118852538.ch15

779 Harris, P.G., 1957. Zone refining and the origin of potassic basalts. Geochim. Cosmochim. Acta 12,
780   195–208. https://doi.org/10.1016/0016-7037(57)90032-7

781 Hartley, M.E., Bali, E., Maclennan, J., Neave, D.A., Halldórsson, S.A., 2018. Melt inclusion
782   constraints on petrogenesis of the 2014–2015 Holuhraun eruption, Iceland. Contrib. Mineral.
783   Petrol. 173. https://doi.org/10.1007/s00410-017-1435-0

784 Herzberg, C., 2011. Identification of Source Lithology in the Hawaiian and Canary Islands:
785   Implications for Origins. J. Petrol. 52, 113–146. https://doi.org/10.1093/petrology/egq075

786 Holness, M.B., Cheadle, M.J., McKenkie, D., 2005. On the Use of Changes in Dihedral Angle to
787   Decode Late-stage Textural Evolution in Cumulates. J. Petrol. 46, 1565–1583.
788   https://doi.org/10.1093/petrology/egi026

789 Holness, M.B., Nielsen, T.F.D., Tegner, C., 2006. Textural Maturity of Cumulates: a Record of
790   Chamber Filling, Liquidus Assemblage, Cooling Rate and Large-scale Convection in Mafic
791   Layered Intrusions. J. Petrol. 48, 141–157. https://doi.org/10.1093/petrology/egl057

792 Holness, M.B., Stock, M.J., Geist, D., 2019. Magma chambers versus mush zones: constraining the
793   architecture of sub-volcanic plumbing systems from microstructural analysis of crystalline
794   enclaves. Philos. Trans. R. Soc. Math. Phys. Eng. Sci. 377, 20180006.
795   https://doi.org/10.1098/rsta.2018.0006

796 Jackson, M.G., Konter, J.G., Becker, T.W., 2017. Primordial helium entrained by the hottest mantle
797   plumes. Nature 542, 340–343. https://doi.org/10.1038/nature21023

798 Jarosewich, E., Nelen, J.A., Norberg, J.A., 1980. Reference Samples for Electron Microprobe
799   Analysis*. Geostand. Geoanalytical Res. 4, 43–47. https://doi.org/10.1111/j.1751-
800   908X.1980.tb00273.x

801 Jochum, K.P., Weis, U., Schwager, B., Stoll, B., Wilson, S.A., Haug, G.H., Andreae, M.O.,
802   Enzweiler, J., 2016. Reference Values Following ISO Guidelines for Frequently Requested
803   Rock Reference Materials. Geostand. Geoanalytical Res. 40, 333–350.
804   https://doi.org/10.1111/j.1751-908X.2015.00392.x

805 Kilbride, B.M., Edmonds, M., Biggs, J., 2016. Observing eruptions of gas-rich compressible magmas
806   from space. Nat. Commun. 7, 13744. https://doi.org/10.1038/ncomms13744

807 Köhler, T.P., Brey, G.P., 1990. Calcium exchange between olivine and clinopyroxene calibrated as a
808   geothermobarometer for natural peridotites from 2 to 60 kb with applications. Geochim.
809   Cosmochim. Acta 54, 2375–2388. https://doi.org/10.1016/0016-7037(90)90226-B

810 Kurz, M.D., Rowland, S.K., Curtice, J., Saal, A.E., Naumann, T., 2014. Eruption Rates for Fernandina
811   Volcano: A New Chronology at the Galápagos Hotspot Center, in: Harpp, K.S., Mittelstaedt,
812   E., d'Ozouville, N., Graham, D.W. (Eds.), Geophysical Monograph Series. John Wiley &
813   Sons, Inc, Hoboken, New Jersey, pp. 41–54. https://doi.org/10.1002/9781118852538.ch4

814 Lissenberg, C.J., MacLeod, C.J., 2016. A Reactive Porous Flow Control on Mid-ocean Ridge
815   Magmatic Evolution. J. Petrol. 57, 2195–2220. https://doi.org/10.1093/petrology/egw074

816   Lissenberg, C.J., MacLeod, C.J., Howard, K.A., Godard, M., 2013. Pervasive reactive melt migration
817   through fast-spreading lower oceanic crust (Hess Deep, equatorial Pacific Ocean). Earth
818   Planet. Sci. Lett. 361, 436–447. https://doi.org/10.1016/j.epsl.2012.11.012
819   Longpre, M.-A., Klugel, A., Diehl, A., Stix, J., 2014. Mixing in mantle magma reservoirs prior to and
820   during the 2011-2012 eruption at El Hierro, Canary Islands. Geology 42, 315–318.
821   https://doi.org/10.1130/G35165.1
822   Lyons, J., Geist, D., Harpp, K., Diefenbach, B., Olin, P., Vervoort, J., 2007. Crustal growth by
823   magmatic overplating in the Galápagos. Geology 35, 511. https://doi.org/10.1130/G23044A.1
824   Matzen, A.K., Baker, M.B., Beckett, J.R., Wood, B.J., Stolper, E.M., 2017a. The effect of liquid
825   composition on the partitioning of Ni between olivine and silicate melt. Contrib. Mineral.
826   Petrol. 172. https://doi.org/10.1007/s00410-016-1319-8
827   Matzen, A.K., Wood, B.J., Baker, M.B., Stolper, E.M., 2017b. The roles of pyroxenite and peridotite
828   in the mantle sources of oceanic basalts. Nat. Geosci. 10, 530–535.
829   https://doi.org/10.1038/ngeo2968
830   Meyer, P.S., Dick, H.J.B., Thompson, G., 1989. Cumulate gabbros from the Southwest Indian Ridge,
831   54S-7 16 E: implications for magmatic processes at a slow spreading ridge. Contrib. Mineral.
832   Petrol. 103, 44–63. https://doi.org/10.1007/BF00371364
833   Mollo, S., Putirka, K., Misiti, V., Soligo, M., Scarlato, P., 2013. A new test for equilibrium based on
834   clinopyroxene–melt pairs: Clues on the solidification temperatures of Etnean alkaline melts at
835   post-eruptive conditions. Chem. Geol. 352, 92–100.
836   https://doi.org/10.1016/j.chemgeo.2013.05.026
837   Naumann, T., Geist, D., 2000. Physical volcanology and structural development of Cerro Azul
838   Volcano, Isabela Island, Galápagos: implications for the development of Galápagos-type
839   shield volcanoes. Bull. Volcanol. 61, 497–514. https://doi.org/10.1007/s004450050001
840   Naumann, T.R., Geist, D.J., 1999. Generation of alkalic basalt by crystal fractionation of tholeiitic
841   magma. Geology 27, 423. https://doi.org/10.1130/0091-
842   7613(1999)027<0423:GOABBC>2.3.CO;2
843   Neave, D.A., Namur, O., Shorttle, O., Holtz, F., 2019. Magmatic evolution biases basaltic records of
844   mantle chemistry towards melts from recycled sources. Earth Planet. Sci. Lett. 520, 199–211.
845   https://doi.org/10.1016/j.epsl.2019.06.003
846   Neave, D.A., Putirka, K.D., 2017. A new clinopyroxene-liquid barometer, and implications for
847   magma storage pressures under Icelandic rift zones. Am. Mineral. 102, 777–794.
848   https://doi.org/10.2138/am-2017-5968
849   Park, J., Morgan, J.K., Zelt, C.A., Okubo, P.G., Peters, L., Benesh, N., 2007. Comparative velocity
850   structure of active Hawaiian volcanoes from 3-D onshore–offshore seismic tomography.
851   Earth Planet. Sci. Lett. 259, 500–516. https://doi.org/10.1016/j.epsl.2007.05.008
852   Peterson, M.E., Saal, A.E., Kurz, M.D., Hauri, E.H., Blusztajn, J.S., Harpp, K.S., Werner, R., Geist,
853   D.J., 2017. Submarine Basaltic Glasses from the Galápagos Archipelago: Determining the
854   Volatile Budget of the Mantle Plume. J. Petrol. 58, 1419–1450.
855   https://doi.org/10.1093/petrology/egx059
856   Pietruszka, A.J., Heaton, D.E., Marske, J.P., Garcia, M.O., 2015. Two magma bodies beneath the
857   summit of Kīlauea Volcano unveiled by isotopically distinct melt deliveries from the mantle.
858   Earth Planet. Sci. Lett. 413, 90–100. https://doi.org/10.1016/j.epsl.2014.12.040
859   Poland, M.P., Miklius, A., Montgomery-Brown, E.K., 2015. Magma supply, storage, and transport at
860   shield stage Hawaiian volcanoes, in: Characteristics of Hawaiian Volcanoes.
861   Poldervaart, A., Hess, H.H., 1951. Pyroxenes in the Crystallization of Basaltic Magma. J. Geol. 59,
862   472–489. https://doi.org/10.1086/625891
863   Putirka, K., 1999. Clinopyroxene + liquid equilibria to 100 kbar and 2450 K. Contrib. Mineral. Petrol.
864   135, 151–163. https://doi.org/10.1007/s004100050503
865   Putirka, K., 1997. Magma transport at Hawaii: Inferences based on igneous thermobarometry 4.
866   Putirka, K.D., 2008. Thermometers and Barometers for Volcanic Systems. Rev. Mineral. Geochem.
867   69, 61–120. https://doi.org/10.2138/rmg.2008.69.3
868   Roeder, P.L., Emslie, R.F., 1970. Olivine-liquid equilibrium. Contrib. Mineral. Petrol. 29, 275–289.
869   https://doi.org/10.1007/BF00371276

870 Shejwalkar, A., Coogan, L.A., 2013. Experimental calibration of the roles of temperature and
871   composition in the Ca-in-olivine geothermometer at 0.1MPa. Lithos 177, 54–60.
872   https://doi.org/10.1016/j.lithos.2013.06.013
873 Sobolev, A.V., Hofmann, A.W., Kuzmin, D.V., Yaxley, G.M., Arndt, N.T., Chung, S.-L.,
874   Danyushevsky, L.V., Elliott, T., Frey, F.A., Garcia, M.O., Gurenko, A.A., Kamenetsky, V.S.,
875   Kerr, A.C., Krivolutskaya, N.A., Matvienkov, V.V., Nikogosian, I.K., Rocholl, A.,
876   Sigurdsson, I.A., Sushchevskaya, N.M., Teklay, M., 2007. The Amount of Recycled Crust in
877   Sources of Mantle-Derived Melts 316, 7.
878 Stock, M.J., Bagnardi, M., Neave, D.A., Maclennan, J., Bernard, B., Buisman, I., Gleeson, M.L.M.,
879   Geist, D., 2018. Integrated Petrological and Geophysical Constraints on Magma System
880   Architecture in the Western Galápagos Archipelago: Insights From Wolf Volcano. Geochem.
881   Geophys. Geosystems 19, 4722–4743. https://doi.org/10.1029/2018GC007936
882 Taracsák, Z., Hartley, M.E., Burgess, R., Edmonds, M., Iddon, F., Longpré, M.-A., 2019. High fluxes
883   of deep volatiles from ocean island volcanoes: Insights from El Hierro, Canary Islands.
884   Geochim. Cosmochim. Acta 258, 19–36. https://doi.org/10.1016/j.gca.2019.05.020
885 Thompson, R., 1987. Phase-equilibria constraints on the genesis and magmatic evolution of oceanic
886   basalts. Earth-Sci. Rev. 24, 161–210. https://doi.org/10.1016/0012-8252(87)90023-7
887 Thompson, R.N., Gibson, S.A., 2000. Transient high temperatures in mantle plume heads inferred
888   from magnesian olivines in Phanerozoic picrites. Nature 407, 502–506.
889   https://doi.org/10.1038/35035058
890 Vidito, C., Herzberg, C., Gazel, E., Geist, D., Harpp, K., 2013. Lithological structure of the Galápagos
891   Plume: Lithological Structure Galpagos Plume. Geochem. Geophys. Geosystems 14, 4214–
892   4240. https://doi.org/10.1002/ggge.20270
893 Vigouroux, N., Williams-Jones, G., Chadwick, W., Geist, D., Ruiz, A., Johnson, D., 2008. 4D gravity
894   changes associated with the 2005 eruption of Sierra Negra volcano, Galápagos.
895   GEOPHYSICS 73, WA29–WA35. https://doi.org/10.1190/1.2987399
896 Villagómez, D.R., Toomey, D.R., Geist, D.J., Hooft, E.E.E., Solomon, S.C., 2014. Mantle flow and
897   multistage melting beneath the Galápagos hotspot revealed by seismic imaging. Nat. Geosci.
898   7, 151–156. https://doi.org/10.1038/ngeo2062
899 Wager, L.R., Brown, G.M., Wadsworth, W.J., 1960. Types of Igneous Cumulates. J. Petrol. 1, 73–85.
900   https://doi.org/10.1093/petrology/1.1.73
901 Welsch, B., Hammer, J., Hellebrand, E., 2014. Phosphorus zoning reveals dendritic architecture of
902   olivine. Geology 42, 867–870. https://doi.org/10.1130/G35691.1
903 White, W.M., McBirney, A.R., Duncan, R.A., 1993. Petrology and geochemistry of the Galápagos
904   Islands: Portrait of a pathological mantle plume. J. Geophys. Res. Solid Earth 98, 19533–
905   19563. https://doi.org/10.1029/93JB02018
906 Wieser, P.E., Edmonds, M., Maclennan, J., Jenner, F.E., Kunz, B.E., 2019. Crystal scavenging from
907   mush piles recorded by melt inclusions. Nat. Commun. 10, 5797.
908   https://doi.org/10.1038/s41467-019-13518-2
909 Wieser, P.E., Edmonds, M., Maclennan, J., Wheeler, J., 2020. Microstructural constraints on
910   magmatic mushes under Kīlauea Volcano, Hawai'i. Nat. Commun. 11, 14.
911   https://doi.org/10.1038/s41467-019-13635-y
912 Winpenny, B., Maclennan, J., 2011. A Partial Record of Mixing of Mantle Melts Preserved in
913   Icelandic Phenocrysts. J. Petrol. 52, 1791–1812. https://doi.org/10.1093/petrology/egr031
914 Wood, B.J., Blundy, J.D., 1997. A predictive model for rare earth element partitioning between
915   clinopyroxene and anhydrous silicate melt. Contrib. Mineral. Petrol. 129, 166–181.
916   https://doi.org/10.1007/s004100050330
917

918

919 # FIGURES
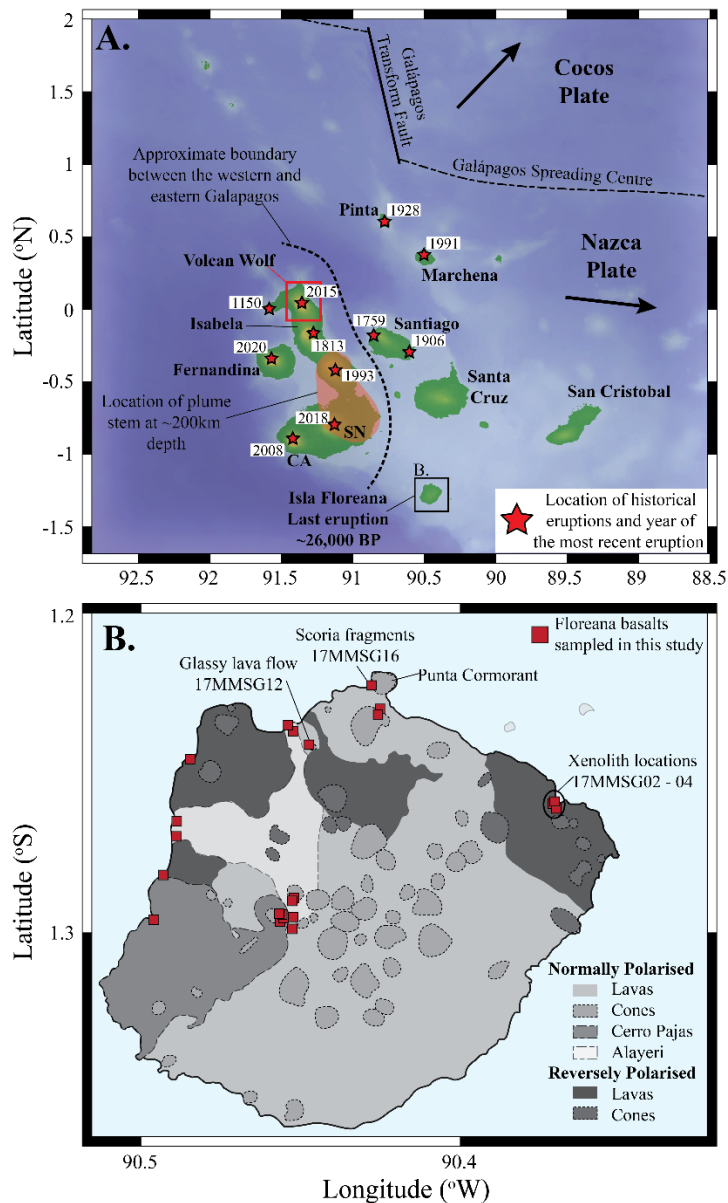
920

921 **Figure 1 - A.** Regional map of the Galápagos Archipelago highlighting the location of Isla Floreana,

922 Cerro Azul (CA), Sierra Negra (SN) and Wolf volcanoes. Dates show the most recent eruptions at

923 historically active volcanic centres. Black arrows show the direction of plate motion for the Nazca and

924 Cocos tectonic plates, respectively. **B.** Geological map of Floreana adapted from Harpp et al. (2014a).

925 Dashed lines delineate monogenetic scoria cones. Normally and reversely polarised lava flows are

926 shown along with the largest (Cerro Pajas) and most recent (Alayeri; ~26,000 years) eruptions on

927 Floreana.

928
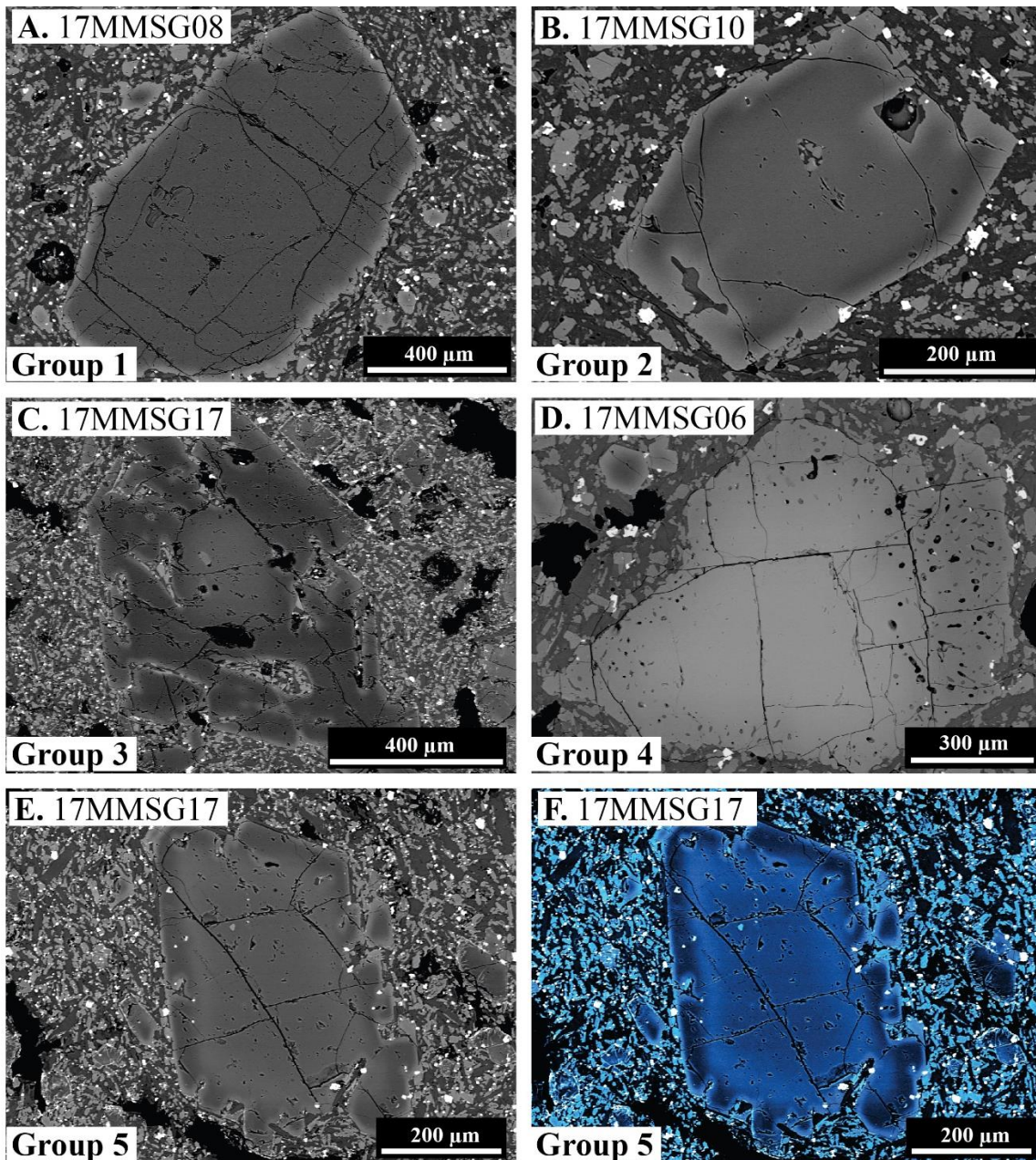
Figure 2 - SEM images of **A.** Group 1 olivines – euhedrual to subhedral crystal morphologies with large, unzoned, crystal cores and narrow, normally-zoned rims. **B.** Group 2 olivines – subhedral to euhedral crystals with clear, reverse-zoning profiles. **C.** Group 3 olivines – skeletal crystals with high forsterite overgrowths on low forsterite cores. **D.** Group 4 olivines – anhedral crystals with sieved textured, reverse zoned rims. **E.** (greyscale) and **F.** (false colour) Group 5 olivines – crystals preserve at least 4 composition zones over ~100-200 µm.

936
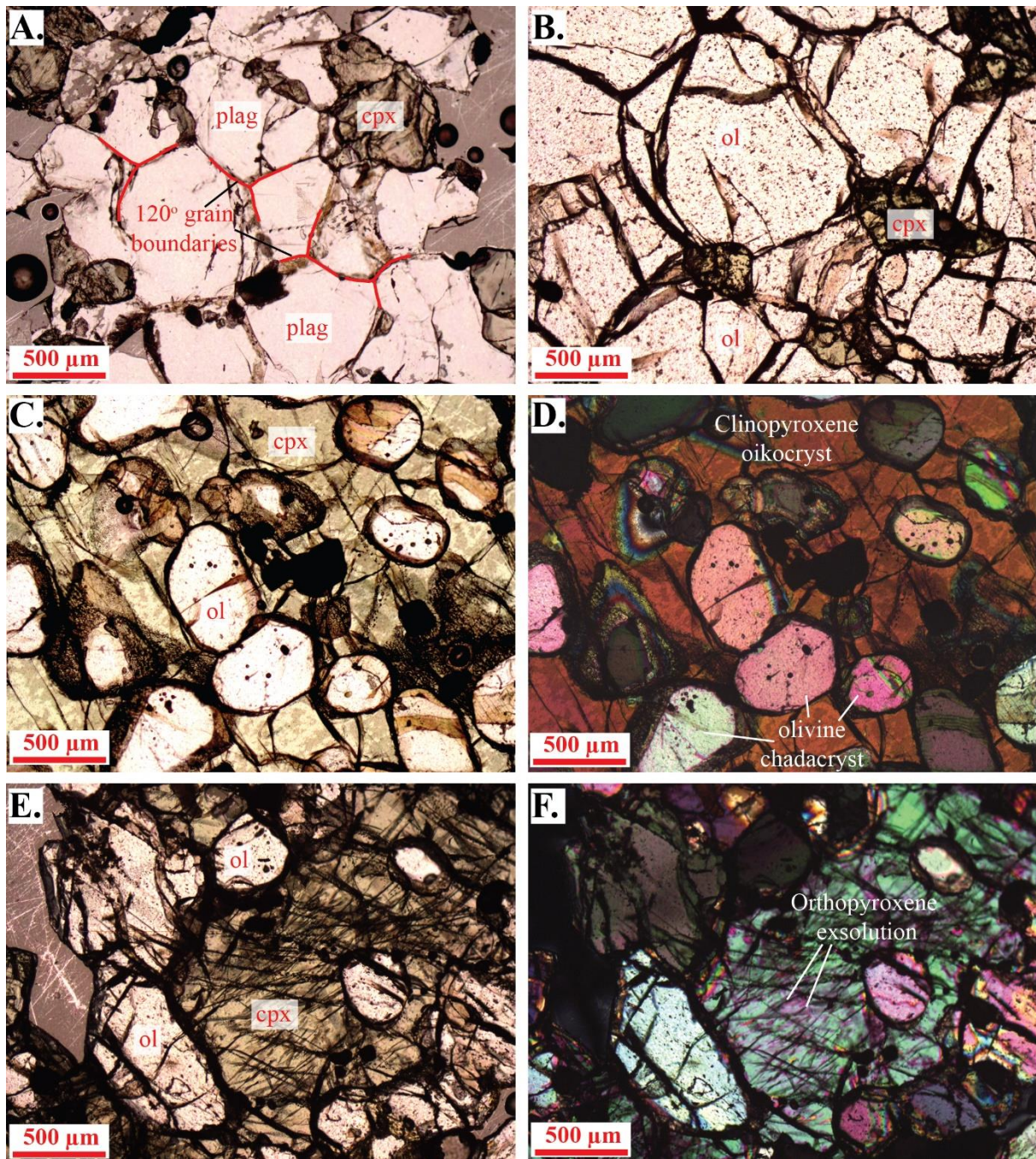
Figure 3 - Plane Polarised Light (**A. – C.** and **E.**) and Crossed Polarised Light (**D., F.**) images of

Floreana xenoliths. **A.** – gabbroic xenolith (17MMSG04b), highlighting near 120° grain boundaries at

monomineralic plagioclase (plag) triple junctions. **B.** – dunitic xenolith (17MMSG04c) with

intercumulus clinopyroxene growth. **C.** and **D.** – wehrlitic xenolith (17MMSG02c) showing a large

clinopyroxene (cpx) oikocryst surrounding olivine (ol) chadacrysts. **E.** and **F.** – wehrlitic xenolith

(sample 17MMSG03a) showing olivine chadacrysts within a clinopyroxene oikocryst. Orthopyroxene

exsolution lamallae are visible within the clinopyroxene.

944
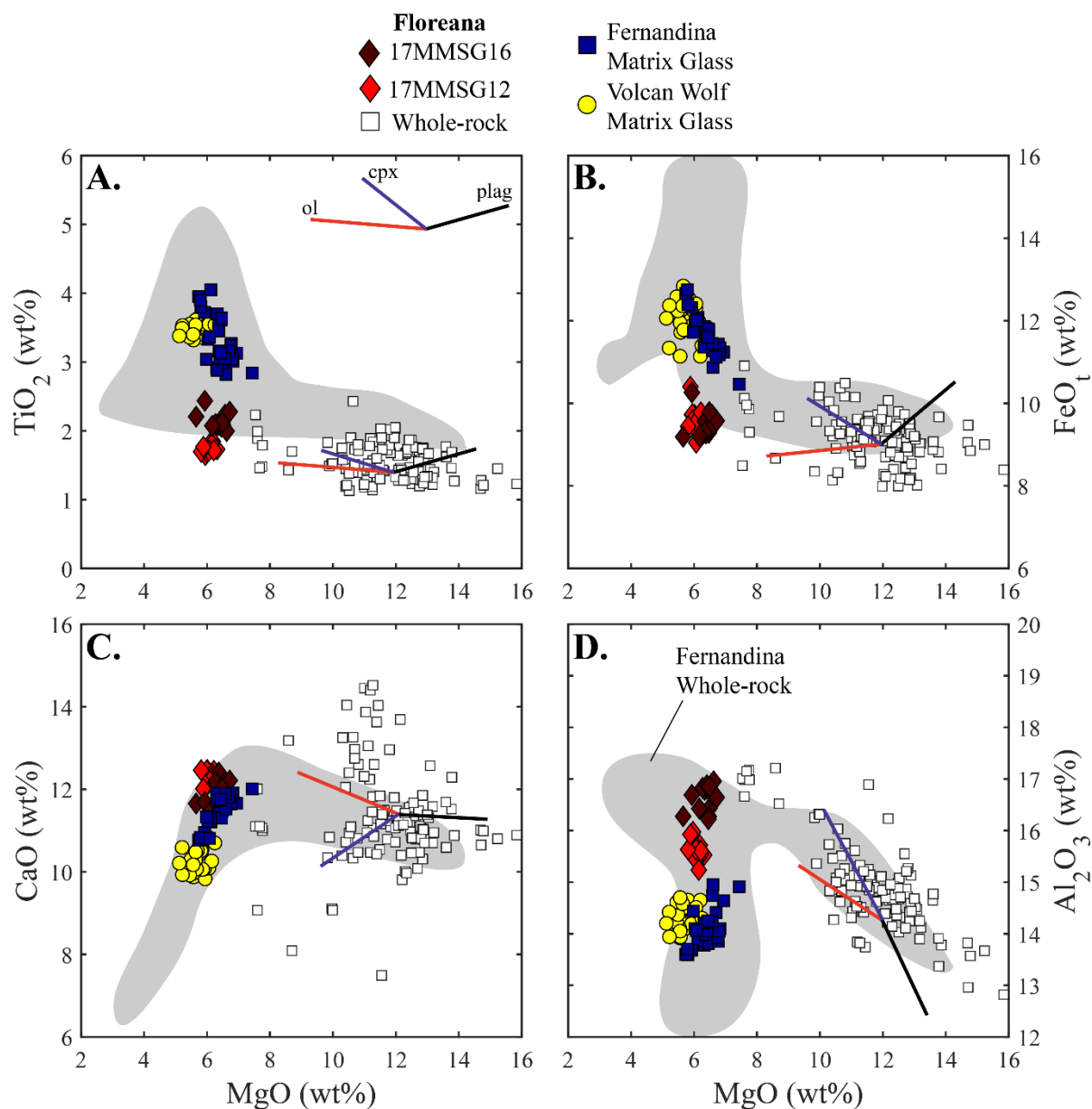
Figure 4 – Major element compositions of matrix glasses (this study) and whole-rocks (Harpp et al.,

2014a) from Floreana, as well as glasses from Fernandina (Peterson et al., 2017) and Wolf volcano

(Stock et al., 2018) in the western Galápagos Archipelago. Lines show trajectories of liquid

compositional evolution olivine (ol; red), clinopyroxene (cpx; blue) and plagioclase (plag; black)

crystallisation. The grey field shows whole-rock data from Isla Fernandina in the western Galápagos

(Allan and Simkin, 2000; Geist et al., 2006). The 2σ precision of our matrix glass analyses is smaller

than the symbol size.

952
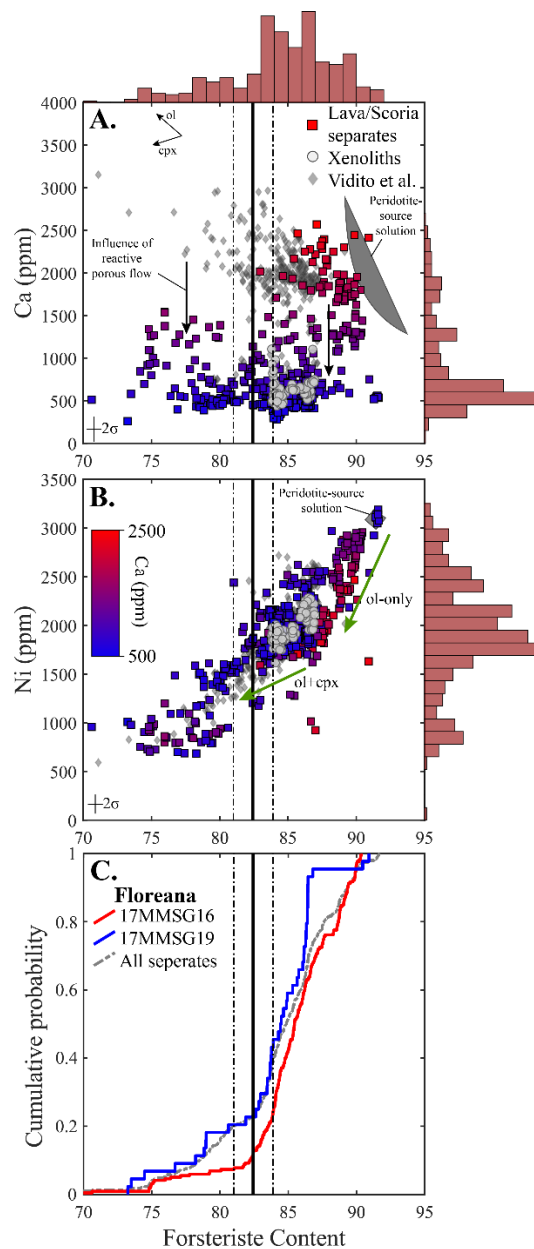
Figure 5 – Major and minor element compositions of olivine crystals from the Isla Floreana basalts. **A**. Fo vs. Ca and **B** Fo vs. Ni in Galápagos olivine crystals with analyses from our lava/scoria separates and xenolith samples, as well as a compilation of available olivine data from Floreana (Vidito et al. 2013). Our lava/scoria analyses are coloured according to their Ca concentration (see colour scale in **B**). The histograms above and to the right of the plots show the data distributions (excluding *in situ* analyses of xenolithic olivines). Peridotite source solutions are taken from Herzberg (2011) and Matzen et al. (2017a). Black arrows in **A.** show the trajectory of crystal compositional evolution during olivine (ol) and clinopyroxene (cpx) crystallisation (taken from Gleeson and Gibson, 2019) and the hypothesised influence of reactive porous flow. The green lines in

B. show the trajectories of crystal compositional evolution during olivine only, followed by olivine + clinopyroxene fractional crystallisation (from Gleeson and Gibson, 2019). **C.** Cumulative probability of forsterite in olivine separates from our lava (17MMSG19) and scoria (17MMSG16) samples. A two-sample Kolmogorov-Smirnov test is used to assess the similarity of the forsterite distributions of the two samples (and all analyses from lava and scoria deposits in this study). Results indicate that the olivine populations from the two samples are drawn from the different distribution (p=0.0021). The vertical black lines show the forsterite compositions of crystals calculated to be in equilibrium with the matrix glass composition of tephra sample 17MMSG16 ($K_d = 0.30\pm0.03$ after Roeder and Emslie, 1970).
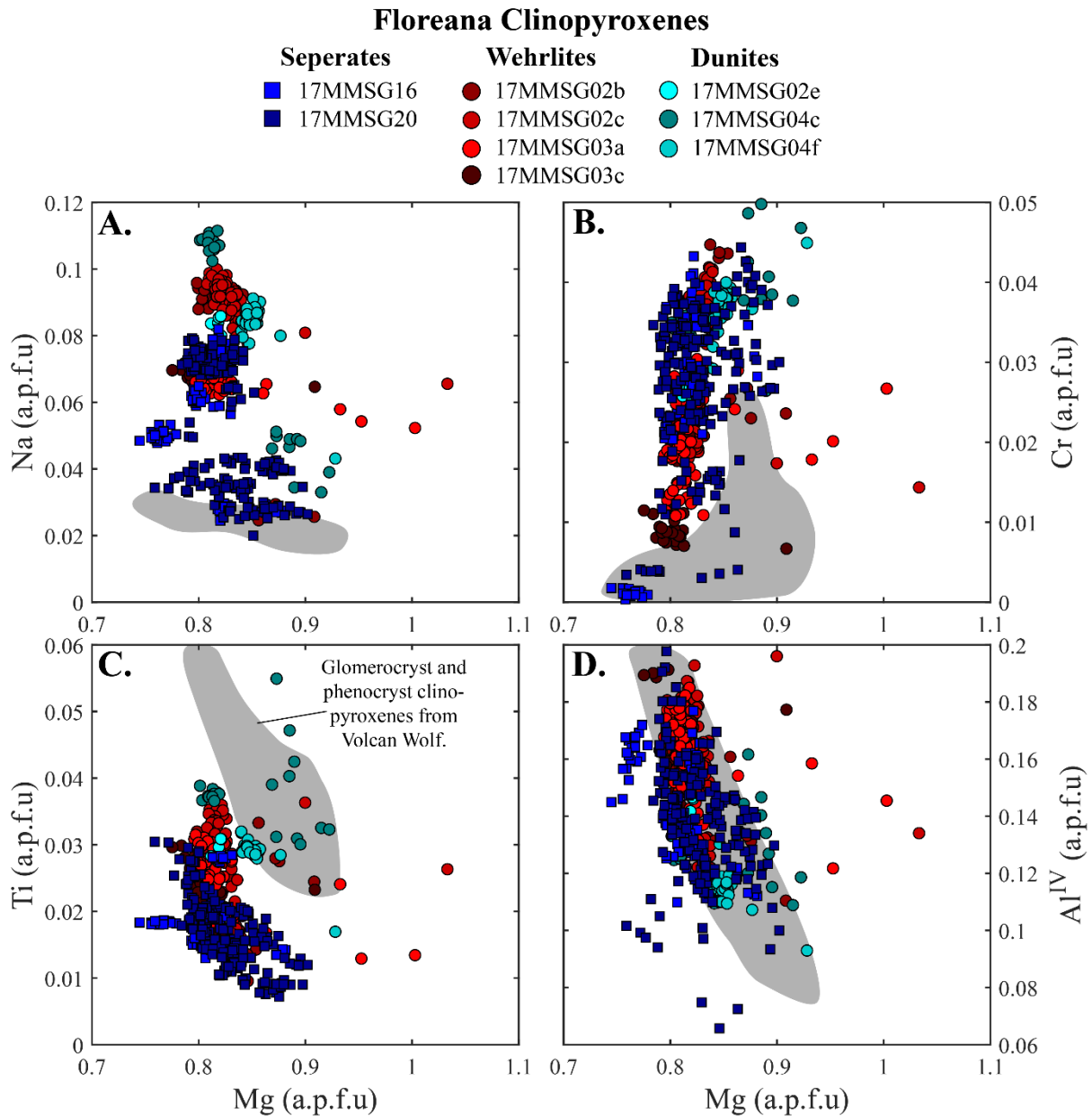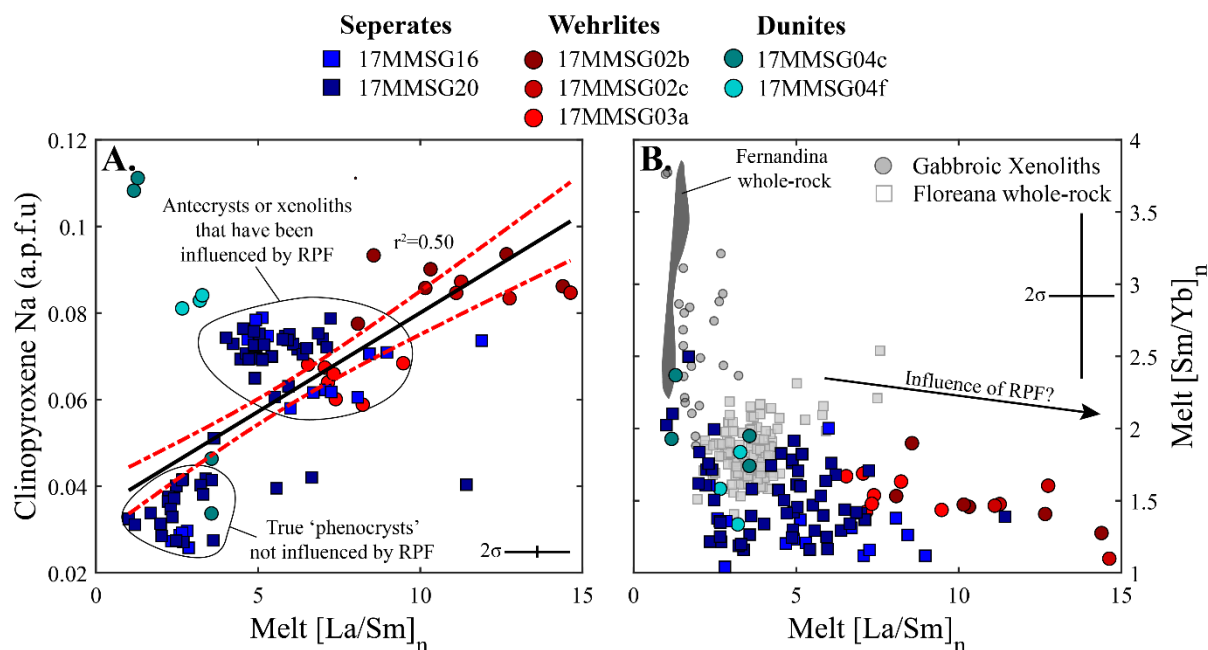
Figure 6 – Major element composition of Floreana clinopyroxenes from our scoria samples and wehrlite and dunite xenoliths. The grey field shows the compositions of clinopyroxenes from Wolf volcano in the western Galápagos Archipelago (from Stock et al. 2018). The 2σ precision of our clinopyroxene analyses is smaller than the symbol size.

Figure 7 – A. $[La/Sm]_n$ vs. Na in clinopyroxenes from our scoria samples and wehrlite and dunite xenoliths. The black line shows a regression through the data ($r^2 = 0.50$) and the red dashed lines show the 95% confidence limits on the regression. **B.** $[La/Sm]_n$ vs. $[Sm/Yb]_n$ of melts calculated to be in equilibrium with our Floreana clinopyroxenes using the model of Wood and Blundy (1997). The black arrow shows the approximate trend of crystal compositional evolution hypothesised to occur as a result of reactive porous flow. The grey field shows whole-rock compositions from Fernandina (Geist et al., 2006; White et al., 1993). **B** additionally shows the whole-rock compositions of erupted Floreana lavas (Harpp et al., 2014a) and analyses of the gabbroic xenoliths from Floreana (this study). Error bars show the fully propagated 2σ precision of our analyses.
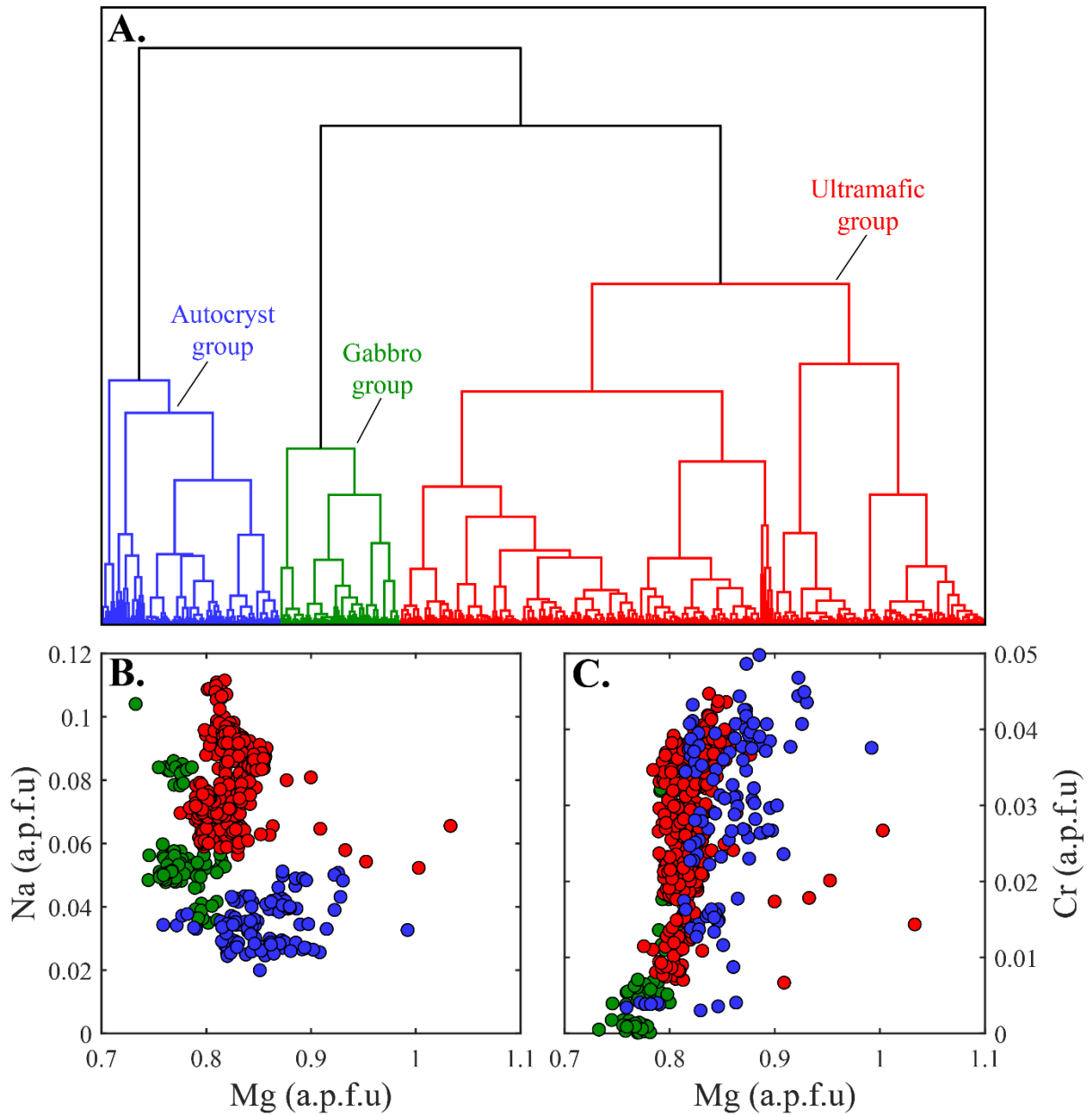
1004

Figure 8 – A. Hierarchical cluster analysis of our clinopyroxene major element analyses. Colours

show the high-level division of crystal compositions into three groups: Group 1 is predominantly

comprised of crystals from wehrlite and dunite xenoliths (red), Group 2 is predominantly comprised

of crystals from gabbroic xenoliths (green) and Group 3 (blue) is dominated by crystals separated

from scoria samples. **B** Na vs Mg and **C** Cr vs Mg in our clinopyroxene analyses from the scoria and

xenoliths, coloured by their group.

1013
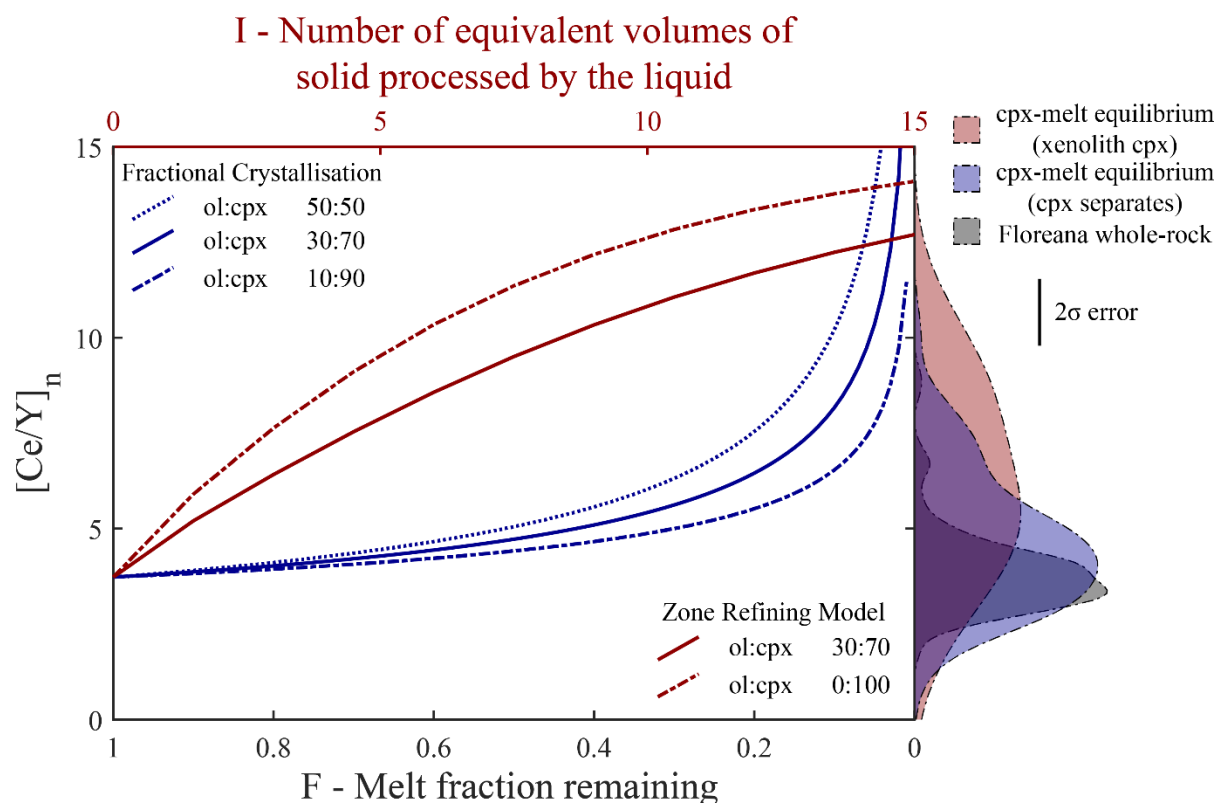
Figure 9 – Models showing the evolution of melt $[Ce/Y]_n$ ratios as a function of the melt fraction

remaining (F) during fractional crystallisation and as a function of the number of equivalent volumes

of solid processed by the liquid (I) during reactive porous flow (red; using the zone-refining model of

Harris, 1957). Line types show how models vary with different ratios of crystallising olivine (ol) and

clinopyroxene (cpx). The kernel density plots to the right show the $[Ce/Y]_n$ density distributions of

liquids calculated to be in equilibrium with clinopyroxene crystals in our wehrlite and dunite xenoliths

(red), scoria samples (blue; 2σ error for the clinopyroxene analyses is shown by the black bar), and

whole-rock analyses of erupted Floreana basalts (grey; Harpp et al., 2014a). Partition coefficients

were calculated for clinopyroxene using the method of Wood and Blundy (1997), the mean major

element composition of the group 3 clinopyroxenes from this study, a temperature of 1225°C, and a

pressure of 700 MPa. Initial Ce and Y concentrations for both models were taken as the mean values

from the whole-rock dataset of Harpp et al. (2014a). Calculation increments are 0.01 in F and 0.1 in I.

1026

1027
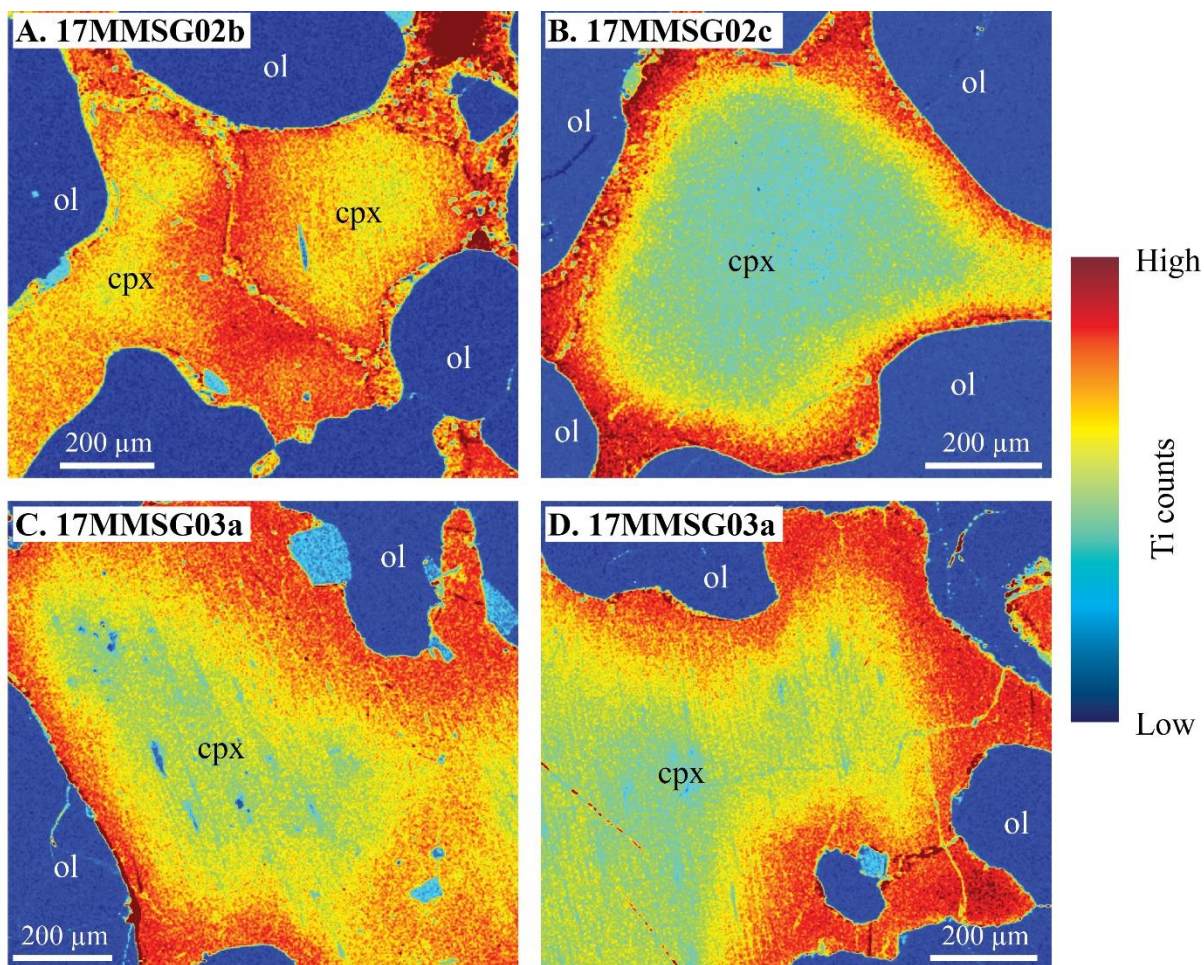
Figure 10 – Ti maps of key clinopyroxene crystals in the Floreana wehrlite xenoliths. These maps display clear zoning in the xenolithic clinopyroxenes with Ti-poor cores and Ti-rich rims. The dark blue regions surrounding clinopyroxene grains are olivine crystals.

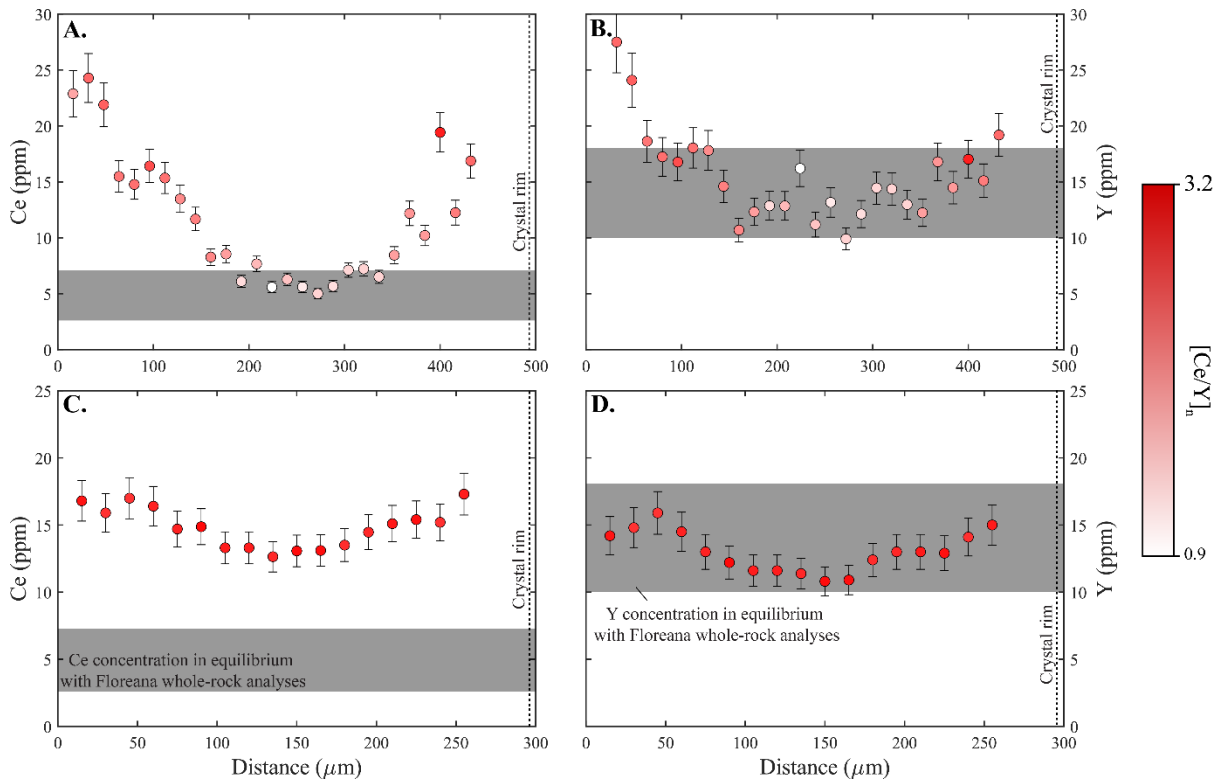**Figure 11** – LA-ICP-MS transects showing Ce (**A, C**) and Y (**B, D**) zoning across two clinopyroxene grains in a wehrlitic xenolith (17MMSG02c). **A.** and **B.** show a transect across the core of a large clinopyroxene oikocryst. **C.** and **D.** show a transect across the apparent core of a smaller clinopyroxene oikocryst. Points are coloured according to their $[Ce/Y]_n$ ratio (see colour scale). The grey bars show the crystal compositions calculated to be in equilibrium with whole-rock analyses of erupted Floreana basalts (Harpp et al., 2014a).
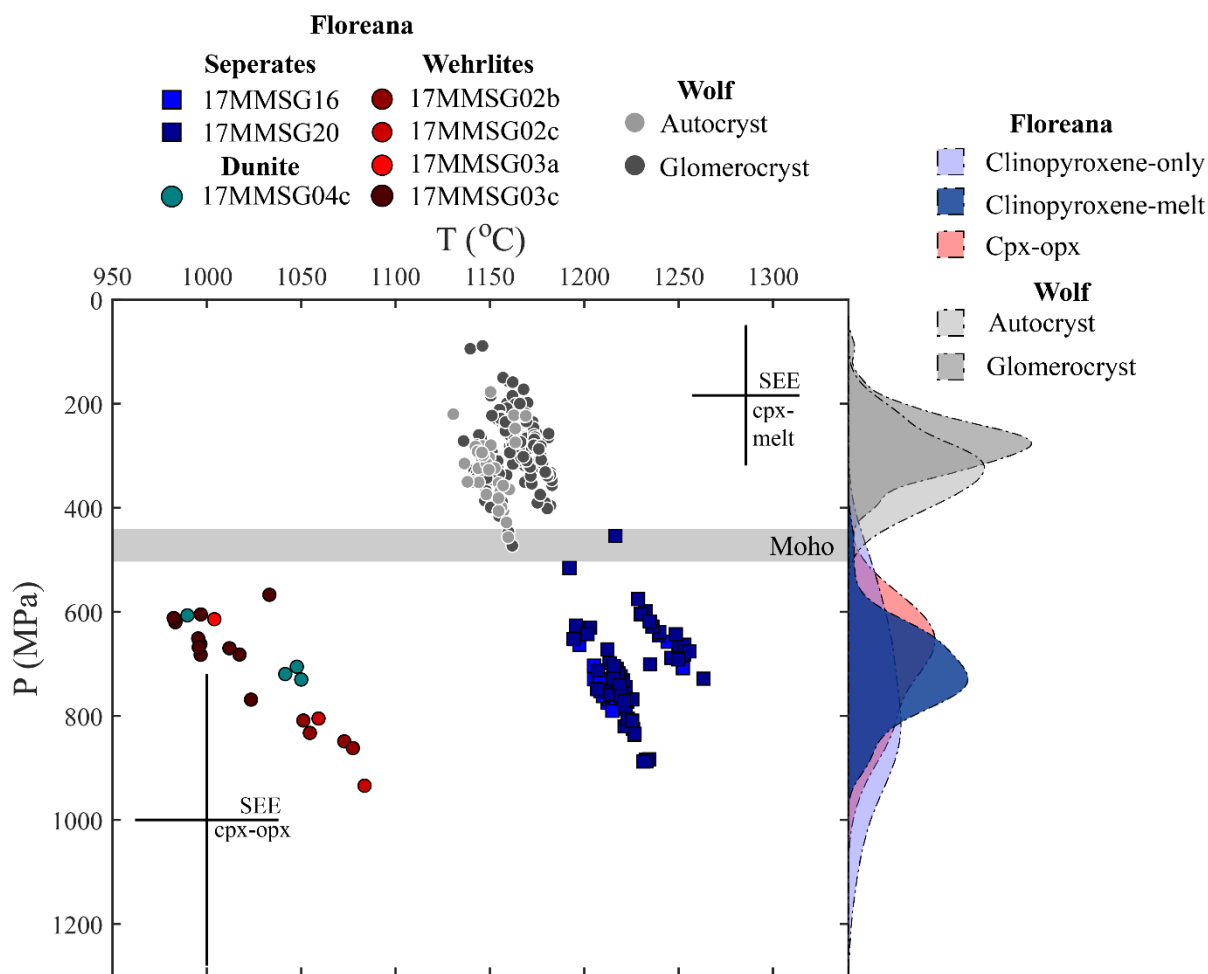
Figure 12 – Petrological thermobarometry results. The kernel density plots to the right show the density distributions of barometric results from different models (light blue – clinopyroxene-only, Putirka (2008); dark blue – clinopyroxene-melt, Neave and Putirka (2017); red – clinopyroxene-orthopyroxene Putirka (2008)). The grey bar shows the Moho depth beneath Fernandina (from Feighner and Richards, 1994) and the grey points and kernel density estimates show clinopyroxene-melt thermobarometric results for autocrysts and glomerocrysts from Wolf volcano for comparison (from Stock et al., 2018).
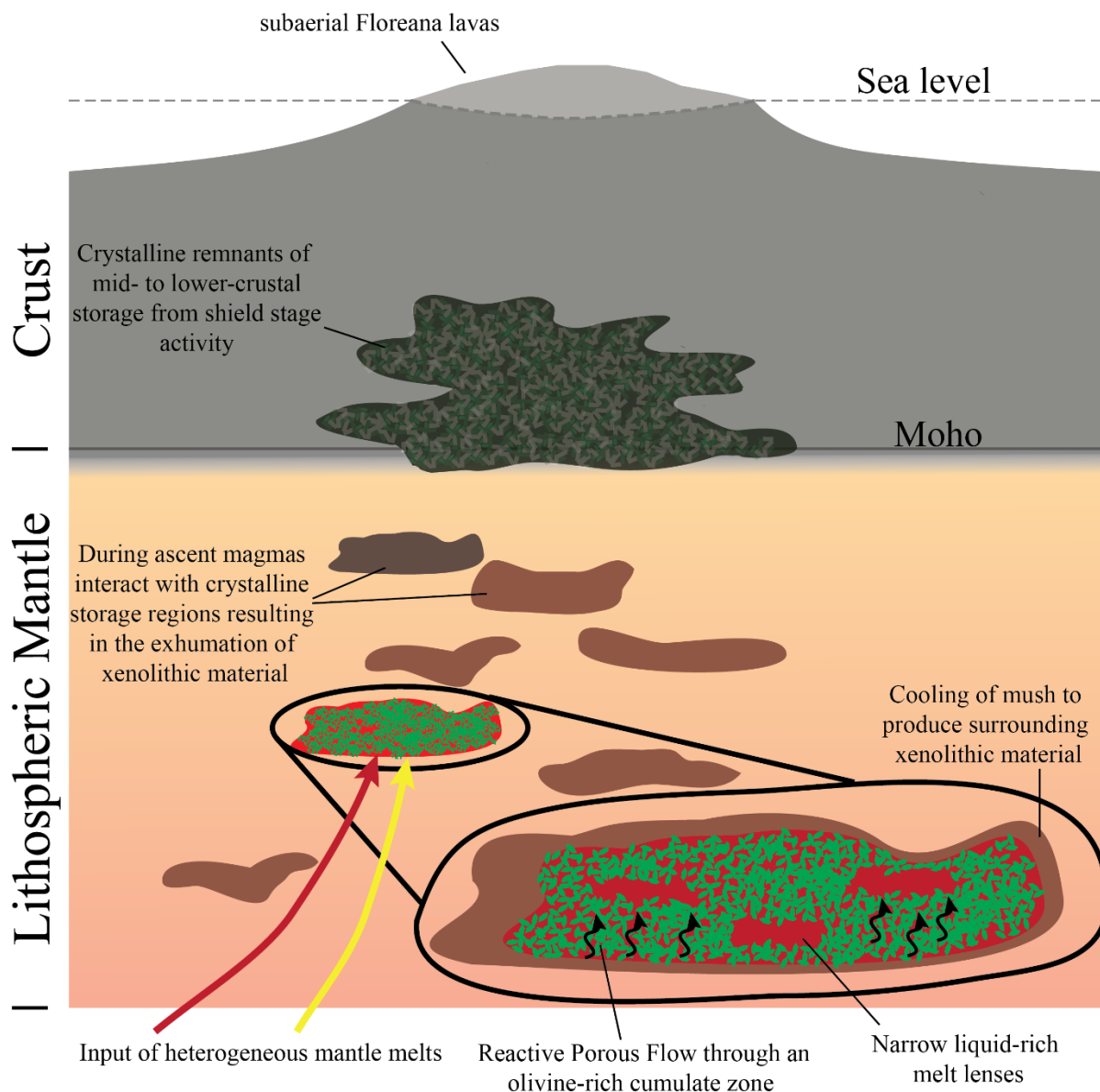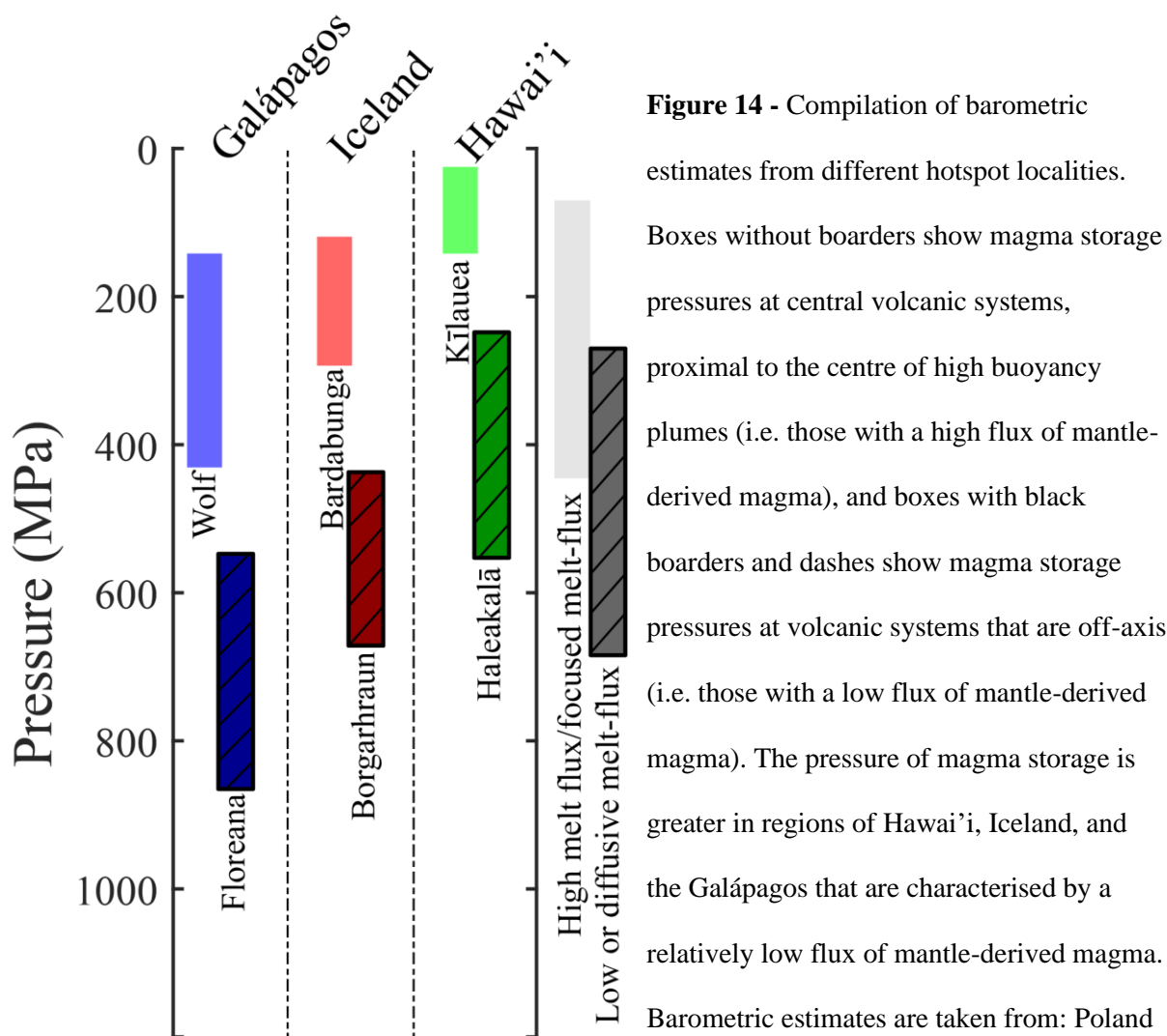
Figure 13 – Schematic illustration of the magma plumbing system beneath Floreana. No magma storage is identified within the crust. Instead, our barometric results indicate that Floreana magmas ascend directly from the upper mantle, where they are stored at a depth of ~23.7 ±5.1 km. Floreana magma storage regions are dominated by crystal-rich domains (i.e. mush). Reactive porous flow is identified as an important mechanism of melt migration and magma differentiation in the crystal-rich storage regions, although our results shows that some crystallisation occurs within liquid-rich domains.

Figure 14 - Compilation of barometric estimates from different hotspot localities. Boxes without boarders show magma storage pressures at central volcanic systems, proximal to the centre of high buoyancy plumes (i.e. those with a high flux of mantle-derived magma), and boxes with black boarders and dashes show magma storage pressures at volcanic systems that are off-axis (i.e. those with a low flux of mantle-derived magma). The pressure of magma storage is greater in regions of Hawai'i, Iceland, and the Galápagos that are characterised by a relatively low flux of mantle-derived magma. Barometric estimates are taken from: Poland et al. (2015) for Kīlauea, using multiple available data streams to create a model of summit magma storage (~25-150 MPa); Hammer et al. (2016) for Haleakalā using clinopyroxene melt barometry (~400 ±160 MPa); Hartley et al. (2018) for Bardabunga using OPAM (210 ±70 MPa); Neave and Putirka (2017) for Borgarhraun using clinopyroxene-melt barometry (570 ±120 MPa); Stock et al. (2018) for Volcan Wolf using OPAM and clinopyroxene-melt barometry (280 ±140 MPa; OPAM results), and this study for Floreana using clinopyroxene-melt barometry (717 ±165 MPa).